Exploring slip partitioning in the Southern Andes: New insights from fault slip data and crustal seismicity

José Cembrano[1], Alain Lavenu[2], Constanza Rojas[3], Pablo Iturrieta[4], Nicolás Pérez-Estay[5], Ashley Stanton-Yonge[6], Javiera Ruz-Ginouves[7], Pamela Pérez-Flores[8], Gerd Sielfeld[9], Gabriela Zañartu[1], Rebecca Pearce[10], Almudena Sánchez de la Muela[11], Tomás Roquer[12], Isabel Santibáñez[13], Tiaren García[14], Flavia Rojas[15], Pablo Sánchez[16], Simone Masoch[6, 17], Thomas Mitchell[18], Gloria Arancibia[1], Ashley Griffith[19], John Browning[18], Karin Hofer[20], Gonzalo Yáñez[1]

(1) *Departamento de Ingeniería Estructural y Geotécnica, Pontificia Universidad Católica de Chile Vicuña Mackenna 4860, Santiago, Chile, jcembrano@uc.cl, garancibia@uc.cl, gyaneza@uc.cl, gabrielazanartu@uc.cl*

(2) *10 rue de Cedres 64110, Gelos, France, alavenu2@orange.fr*

(3) *Parcela 3, Camino El Yeco Tunquen, ruta F814, Algarrobo, Chile, corojas1@gmail.com*

(4) *GFZ Helmholtz Centre for Geosciences, Potsdam, Germany, pciturri@gfz.de*

(5) *Department of Earth Ocean and Atmospheric Science, University of British Columbia, Vancouver, Canada, nnperezestay@eoas.ubc.ca*

(6) *Università degli Studi di Padova, Dipartamento di Geoscienze, Via Giovanni Gradenigo, 6, 35131 Padova PD, Italia, ashley.sesnic.18@ucl.ac.uk*

(7) *Department of Geology, University of Otago, 360 Leith Street, Dunedin, New Zealand, javiera.ruz@postgrad.otago.ac.nz*

(8) *CIGEA (Consultoría Geológico Ambiental Ltda.), Manuel Rojas 23 Terrazas de Amancay, Huasco, Chile, pperezflores@gmail.com*

(9) *University of Auckland, Faculty of Science, 23 Symonds Street 1010, Auckland, New Zealand gerd.sielfeld@auckland.ac.nz*

(10) *Royal Roads University, Cascade Institute, 2005 Sooke Rd, Victoria, Canada. pearce@cascadeinstitute.org*

(11) *Consejo Superior de Investigaciones Científicas, Instituto Geológico y Minero de España, Departamento de Riesgos Geológicos y Cambio Climático, Ríos Rosas 23, Madrid, España. asmgarzon@ucm.es*

(12) *Departamento de Ingeniería de Minas, Metalurgia y Materiales, Universidad Técnica Federico Santa María, Av. Vicuña Mackenna 3939, Santiago, Chile. tomas.roquer@usm.cl*

(13) *Las Hortensias 2546, Santiago, isantiboric@gmail.com*

(14) *SRK Consulting Chile, Hydrogeology Area, Vitacura 2939, 9th floor, Santiago, Chile. tiaren.garcia@gmail.com*

(15) *University of Manchester, Department of Earth and Environmental Sciences, Oxford Road M13 9PL, Manchester, UK. flavia.rojasguzman@manchester.ac.uk*

(16) *Universidad Austral de Chile, Facultad de Ciencias, Avenida Rector Eduardo Morales Miranda s/n, Valdivia, Chile. pablo.sanchez@uach.cl*

(17) *Nevada Seismological Laboratory, University of Nevada, Reno, USA. smasoch@unr.edu*

(18) *University College London, Department of Earth Sciences, Gower Street, London, UK, Thomas Mitchell, j.browning@ucl.ac.uk*

(19) *School of Earth Sciences, The Ohio State University, 43210, Columbus, Ohio, USA. griffith.233@osu.edu*

(20) *Swiss Federal Institute of Technology in Lausanne (EPFL), Lausanne, Switzerland, karin.hoferapostolidis@epfl.ch*

Abstract

Active slip partitioning between the subduction megathrust and the upper plate is investigated in the oblique-convergence setting of the Nazca-South American plate boundary between 33° and 47° S. This segment has two major along-strike bends: the Maipo Orocline (~34° S) and the Arauco Peninsula (~38° S), whereas south of 38° S, lies the intra-arc Liquiñe-Ofqui Fault System (LOFS). Here we examine long- and short-term upper-plate deformation by combining a harmonized catalog of about 2,300 fault-slip measurements in the forearc and arc regions, from which we derive P-T axes using kinematic inversions, along with an integrated seismological database for upper-plate events (1976-2025), including global and local networks. These data are categorized by forearc, arc, and back-arc regions. We identify four distinct tectonic segments based on the spatial distribution of P and T axes in the long-and short-term: (1) 33°–34° S, showing both ~E–W and ~N–S subhorizontal shortening in the forearc and arc areas, suggesting active radial shortening; (2) 34°–37° S, dominated by mostly blind, seismogenic, margin-parallel dextral faults along with NW- and NE-trending structures running at a high angle with respect to the plate margin (called transverse faults here); (3) 37°–41° S, where margin-orthogonal subhorizontal shortening in the submerged forearc coexists with nearly margin-parallel shortening in the emerged forearc, with contemporaneous dextral slip along the LOFS and ~E–W shortening accommodated by transverse NE-trending dextral and NW-trending sinistral seismically active faults; and (4) 41°–47° S, a region governed mainly by the geometry and kinematics of the LOFS strike-slip duplex. Kinematic indicators on mesoscopic faults (mostly slickenfibers) and a lack of pseudotachylytes suggest a considerable aseismic component to upper-plate fault slip, implying that morphotectonic slip rates may overestimate seismic hazard.

Future detailed geodetic data may help better constrain the relative contributions of aseismic and seismic slip on the upper-plate faults in this Andean segment.

Resumen

Explorando la partición del deslizamiento en los Andes del Sur: Nuevas perspectivas a partir de datos de deslizamiento de fallas y sismicidad cortical. La partición del vector de convergencia entre la zona de subducción y la placa superior es analizada en el contexto de la convergencia oblicua entre las placas de Nazca y Sudamérica, desde los 33° S hasta los 47° S. Este segmento presenta dos marcadas curvaturas en el margen continental: el Oroclino de Maipo (~34° S) y la Península de Arauco (~38° S), mientras que al sur de los 38° S se desarrolla, en el dominio de intra-arco, el Sistema de Fallas Liquiñe-Ofqui (SFLO). En este trabajo se examina la deformación de la placa superior mediante un catálogo de aproximadamente 2.300 mediciones de fallas en las regiones del antearco y del arco, junto con datos sismológicos de eventos entre 1976 y 2025, procedentes de redes globales y locales, categorizados como de antearco, arco y trasarco. Se identifican cuatro segmentos tectónicos con base en la distribución espacial de los ejes P y T: (1) 33°–34° S, con acortamiento subhorizontal en direcciones ~E-O y ~N-S, lo que sugiere acortamiento radial; (2) 34°–37° S, dominado por fallas dextrales, en su mayoría ciegas, sismogénicas y paralelas a la margen, junto con estructuras sismogénicas de rumbo NO y NE; (3) 37°–41° S, donde coexiste un acortamiento ortogonal al margen en el antearco sumergido con otro paralelo al margen en el antearco emergido. Adicionalmente, ocurren fallas transversales sísmicamente activas, NO y NE, sinistrales y dextrales, respectivamente; y (4) 41°–47°, una región gobernada principalmente por la geometría y cinemática del SFLO. Indicadores

cinemáticos en fallas mesoscópicas (e.g., fibras de crecimiento) y la ausencia de pseudotaquilitas sugieren una componente asísmica significativa, lo que puede llevar a sobreestimar el peligro sísmico calculado mediante estimaciones morfotectónicas. Futura información geodésica de detalle puede contribuir a discriminar de mejor manera el deslizamiento sísmico del asísmico en las fallas de la placa superior de este segmento de los Andes.

INTRODUCTION

The partitioning of upper plate deformation at obliquely convergent margins has been studied for over fifty years (e.g., Fitch, 1972; Jarrard, 1986; Beck, 1991; McCaffrey, 1992, 1996; Canora et al., 2014; Stanton-Yonge et al., 2016). Early research by Fitch (1972) proposed that the oblique convergence vector is partitioned into margin-orthogonal and margin-parallel slip components, with the former mainly accommodated by the subduction zone and the latter by an intra-arc strike-slip fault system within the upper plate. Beck (1991) and McCaffrey (1992) provided important insights by suggesting that most obliquely convergent margins only show partial slip partitioning, where only part of the oblique convergence is absorbed by oblique displacement at the plate boundary, leading to a smaller residual margin-parallel slip vector than otherwise assumed in earlier studies. Some years later, de Saint Blanquat et al. (1998) refined earlier deformation and slip partitioning models by proposing a conceptual framework for transpressional magmatic arcs as a general model for obliquely convergent margins (Teyssier et al., 1995). In their model, they define margin-parallel domains in the upper plate that accommodate not only one component of the convergence vector but different degrees and combinations of strike-slip and shortening deformation (Fig. 1). This framework was further improved

and applied to the specific case of the Southern Andes by Lavenu and Cembrano (1999).

Recent seismological studies in the Chilean margin have suggested that the accommodation of the margin-parallel component of the plate convergence vector within the upper plate is more complex than previously understood (e.g., Sielfeld et al., 2019a; Pérez-Estay et al., 2020). These studies revealed significant variations in earthquake focal mechanisms within the brittle crust of the continental plate, in both kinematics and orientations. Structural geology studies have independently reported similar behavior in the long-term deformation recorded in exhumed faults, suggesting that the margin-parallel component is accommodated by numerous reactivated and new faults with varying strike, dip, and kinematics, many of which show evidence of activity from the Pliocene to the Quaternary (Pérez-Flores et al., 2016; Sielfeld et al., 2017). Numerical models support these field observations, highlighting the importance of fault strike relative to the margin and showing that a range of fault kinematics can coexist to accommodate the margin-parallel slip component (Stanton-Yonge et al., 2016). Analog models of the Southern Andean oblique subduction plate margin are consistent with these observations as well (e.g., Eisermann et al., 2021).

Overall, evidence from seismology, structural geology, and numerical modeling suggests that slip complexity involves not only margin-parallel faults but also transverse faults, which significantly contribute to accommodating fault slip in the upper plate. In this study, we present a review of the existing published seismological and field structural data for the Southern Andes between 33° and 47° S, a segment marked by the end of flat subduction in the north (e.g., Jordan et al.

1983) and the Chile Triple Junction in the south (e.g., Forsythe and Nelson, 1985). This continental segment features two sharp inflections of the plate margin, one at ~34° S (Maipo Orocline) and another around 38° S (Arauco Peninsula) (Fig. 2). Notably, two significant earthquake rupture zones associated with subduction megathrust earthquakes overlap at the Arauco Peninsula: the 2010 Maule earthquake and the 1960 Valdivia earthquake (e.g., Moreno et al., 2009, 2012; Vigny et al., 2011). This latter region therefore represents a critical tectonic element of the plate margin (e.g., Melnick et al., 2009), marking a slight but significant change in plate obliquity (e.g., Stanton-Yonge et al., 2016) (Fig. 2).

In this manuscript, we aim to improve our understanding of how deformation and slip resulting from oblique plate convergence are accommodated in the upper plate. Our newly integrated structural and seismological evidence strongly suggests the existence of four consecutive Andean segments that have experienced unique tectonic evolution since the Neogene. This segmentation offers important insights into the fundamental mechanisms underlying plate margin deformation and the seismic hazards (and possible risks) associated with potentially seismogenic faults.

2. TECTONIC AND GEOLOGICAL SETTING

2.1. Geology and crustal structure of the Southern Andes

The Andean mountain range between 33° and 47° S shows a slightly deformed, rigid, and cold forearc region adjacent to a weaker and hotter magmatic arc domain (e.g., Tassara and Yáñez, 2003; Farías et al., 2006; Cembrano and Lara, 2009; Gerbault et al., 2009). This segment is characterized by a slightly dextral-oblique convergence between the Nazca and South American plates, occurring at a rate of approximately 7 cm/year (e.g., Angermann et al.; 1999; Quiero et al., 2022). Oblique

169 convergence has been dominant at the plate margin for the past ~20 Myr (Pardo-
170 Casas and Molnar, 1987; Somoza, 1998), with slight transient variations in the
171 obliquity angle (<10°) on timescales of a few Myr (Quiero et al., 2022). The southern
172 boundary of the study region is defined by the Chile Triple Junction, where the active
173 Chile Ridge, which separates the Nazca plate from the Antarctic plate, is subducted
174 beneath the continent (Figs. 2 and 3).

175 The regional geological units between 33° and 47° S form belts roughly parallel to
176 the margin, from Paleozoic plutonic, volcano-sedimentary, and metamorphic rocks in
177 the forearc to Meso-Cenozoic plutonic and volcano-sedimentary formations in the
178 arc and back-arc regions (Fig. 2). In between, scattered outcrops of Oligocene-
179 Miocene rocks, predominantly obscured by more recent volcano-sedimentary
180 deposits, are present (Fig. 2).

181 Between 33° and 38° S, the basement rock units of the volcanic arc consist primarily
182 of extensive outcrops of Meso-Cenozoic volcanic and volcano-sedimentary rocks,
183 locally intruded by Neogene plutons (e.g., Charrier et al., 2002; Farías, et al., 2007;
184 Piquer et al., 2010; Pearce et al., 2020) (Fig. 2). This setting dramatically changes
185 south of ~38° S, where volcanoes are mostly constructed directly on top of Meso-
186 Cenozoic plutonic rocks (Hervé et al. 1994; Stern et al. 2011) (Fig. 2). Consistently,
187 Cenozoic regional exhumation rates, determined using both apatite and zircon
188 fission track data along the main range, show a sharp increase at around 38° S.
189 There, exhumation rates jump from <0.1 mm/year in the north to >1 mm/year to the
190 south (e.g., Thompson, 2002; Glodny et al., 2008).

191 Moreover, the crustal thickness beneath the magmatic arc steadily decreases from
192 approximately 55 km at 33° S to 35 km at 46° S, paralleled by a decline in the

193 average elevation of the Main Cordillera, from 5,000 m to under 2,000 m (Tassara
194 and Yáñez, 2003; Cembrano and Lara, 2009).

195 **2.2. Short-term slip partitioning**

196 To characterize the short-term crustal deformation between 33° and 47° S, we
197 compiled a comprehensive focal-mechanism catalog of Mw>5.0 earthquakes in the
198 upper plate, spanning the entire forearc, arc and back-arc regions (Fig. 2). Compiled
199 from global network sources, the catalog aims to provide a present-day snapshot of
200 the state of stress and slip partitioning along and across the plate boundary.
201 Relevant (Mw>7.0) subduction earthquakes were also recorded (Stanton-Yonge et
202 al., 2016), enabling the calculation of the margin-parallel component of oblique
203 subduction and its variation along strike (Fig. 2).

204 The dataset was constructed by integrating focal-mechanism solutions from the
205 Global Centroid Moment Tensor (GCMT; Ekström et al., 2012) and the Advanced
206 National Seismic System Comprehensive Catalog (ANSS-ComCat; U.S. Geological
207 Survey, 2017), harmonizing them into a unified format and retaining events within the
208 study area from 1976 to 2025. Events were filtered, merged, and checked for
209 duplicates (e.g., Weatherill et al., 2016), and supplemented with relocated
210 hypocenters where available (Potin et al., 2025). Using slab interface geometry
211 (Hayes et al., 2018) and kinematic criteria similar to those applied in the New
212 Zealand Seismic Hazard Model (e.g., Gerstenberger et al., 2024), we classified
213 events into forearc, intra-arc, and back-arc domains. The classification criteria and
214 the full catalog, further divided into intra-slab, outer-rise, and deep earthquakes, are
215 detailed in figure S1 of the Supplementary Material. The P- and T-axes of
216 earthquakes for each class are shown in figure S2 of the Supplementary Material.

More information regarding data processing and accessibility is provided in the Data and Resources chapter at the end of this manuscript.

The seismicity related to the subduction interface exhibits reverse-slip and involves ~N–S striking nodal planes with P-axes trending nearly E–W (Fig. 2). This indicates a P-axis direction slightly rotated clockwise (~10-20°) from the plate margin slip vector (Stanton-Yonge et al., 2016).

In the submerged forearc (west of the coastline), the seismicity is focused in the rupture zones of the Mw 8.8 2010 Maule and Mw 8.0 1985 Valparaíso earthquakes (Fig. 2). Most of these events (41 out of 49; ~84%) are aftershocks of the 2010 megathrust earthquake, and can be grouped into three populations: (1) 37 reverse-slip events with nodal planes striking near N–S and P-axes trending close to E-W, similar to the subduction-related events; (2) nine normal-slip events with nodal planes striking NW, NS, and NE; and (3) three strike-slip events with margin-oblique nodal planes and P-axes trending NE (Fig. 2).

In the emerged forearc (east of the coastline), 23 earthquakes (12 of which occurred before the 2010 Maule earthquake) can be grouped as follows: (1) 11 with margin-oblique nodal planes along the entire margin, either with strike-slip (three), reverse/strike-slip (six), or normal/strike-slip (two) kinematics, exhibiting margin-subparallel P-axes trending from N–S to NE; (2) six normal-slip earthquakes with nodal planes striking near NW and near N–S, five of which are associated with the Mw 6.9 2010 Pichilemu aftershock sequence (e.g., Aron et al., 2013); and (3) six reverse-slip events with nodal planes striking mainly N–S (Fig. 2).

Intra-arc seismicity (28 events) is primarily represented by strike-slip events (Fig. 2), with two exceptions: the normal, dip-slip, Mw 6.1 2007 Aysén earthquake, located at

45.4° S (Legrand et al., 2011), and three reverse-slip earthquakes at 34°, 35°, and 42° S. In the northern part of the study region, between 33° and 34° S, strike-slip events have a nearly E–W oriented horizontal P-axis, with NW- and NE-striking nodal planes, exhibiting sinistral or dextral kinematics, respectively. Between 34° and 37° S, earthquakes show strike-slip kinematics with subvertical nodal planes striking approximately N25°E (dextral) and N65°W (sinistral). South of 37° S, the events show strike-slip kinematics, with nodal planes striking between N20°W and N30°E, mostly oriented from N–S to N10°E. Earthquake kinematics within the southern part of the arc maintain a consistent orientation, characterized by a subhorizontal, NE-trending P-axes, as also documented by local seismological networks (Lange et al., 2008; Pérez-Estay et al., 2020).

2.3. Long-term slip partitioning

The long-term regional-scale structure of the intra-arc and back-arc domains between 33° and 35° S is defined by east-verging, margin-parallel folds and thrusts of Cenozoic age, representing the westernmost part of the Aconcagua and Malargüe foreland fold-and-thrust belts (e.g., Giambiagi and Ramos, 2002). Major regional reverse faults affect the Meso-Cenozoic volcano-sedimentary units, accommodating a limited degree of shortening compared to the Andes of northern Chile (Giambiagi et al., 2012). A similar intra-arc compression regime has been seismically recorded in the 33°-34° S latitude range (Ammirati et al., 2022).

Available fault-slip data document the long-term stress and strain state of the forearc and intra-arc regions since the Pliocene, revealing a local margin-parallel shortening in the forearc and a NE-trending, subhorizontal maximum compression axis (σ_1) across the volcanic arc, the latter prevalent from 37° to 46° S (e.g., Arancibia et al.,

1999; Lavenu and Cembrano, 1999; Cembrano et al., 2000; Lara et al., 2006). In the arc domain, the main compressional stress axis aligns with many volcanic features and dike trends (Cembrano and Lara, 2009; Sielfeld et al., 2017), a pattern that is also consistent with contemporaneous margin-parallel dextral strike-slip deformation.

Although margin-parallel reverse faults dominate, there is evidence of conjugate NE-striking dextral and NW-striking sinistral strike-slip faults in the forearc (Aron et al., 2013; Santibáñez et al., 2019), the magmatic arc (e.g., Rivera and Cembrano, 2000; Piquer et al., 2015, 2021), and the foreland (Mescua et al., 2019; Olivar et al., 2022). The major earthquakes recorded between 34–37° S (Mw>6), namely the Mw 6.5 2004 Teno and the Mw 6.0 2012 El Melado, have strike-slip focal mechanisms, confirming the seismogenic nature of the NE- and NW-trending faults in this area (e.g., Sielfeld et al., 2019b). Moreover, these arc-oblique fault systems have been proposed as structural controls on magmatism and mineralization (e.g., Piquer et al., 2015).

Between 36° and 38° S, the Argentine foreland is characterized by the Neogene Chos-Malal and El Agrio fold-and-thrust belts (e.g., Folguera et al., 2004, 2007), with active back-arc volcanism coeval with E-W compression along the El Agrio belt (e.g., Galland et al., 2007). In contrast, the arc region, which lies within a fairly similar latitude range, has undergone arc-orthogonal extension during the Quaternary, accompanied by a minor component of dextral strike-slip displacement (Melnick et al., 2006).

West of the El Agrio lies the Antiñir-Copahue fault zone, an east-vergent, high-angle fault system characterized by dextral transpressive and dextral transtensive faults, which forms the orogenic front at these latitudes (Folguera et al., 2004). This fault

zone merges southwestwards with the 1200 km-long Liquiñe-Ofqui Fault System (LOFS), a major intra-arc fault system that extends from 38° to 47° S (Hervé, M., 1976; Hervé et al., 1979; Hervé, 1994; Cembrano et al., 1996; Folguera et al., 2002; Rosenau et al., 2006; Pérez-Flores et al., 2016; Sielfeld et al., 2019a). Evidence from ductile-to-brittle shear zones suggests that the LOFS has been active as a transpressional dextral strike-slip structure for at least the past 6 Myr (Arancibia et al., 1999; Cembrano et al., 2002), and that it may have acted as a leaky transform fault ~25 Ma ago (Hervé et al., 1995). This fault was believed to be spatially and genetically linked to sedimentation, local magma ascent, and concomitant pillow lava formation under a deep-rooted transtensional regime (Hervé et al., 1995). The shortening component of Pliocene-to-recent intra-arc deformation increases to the south as the LOFS approaches the Chile Triple Junction (e.g., Lavenu and Cembrano, 1999; Cembrano et al., 2002; Thompson, 2002; Rosenau et al., 2006).

In the study area, a landmark paper providing an overview of different stress states associated with individual volcanoes is that of Pérez-Estay et al. (2023). The study used available fault-slip data and earthquake focal mechanisms to classify volcanoes by their stress states. A key conclusion is that the stress regime along the arc is neither uniform nor of a single type; instead, it exhibits a spatial and/or temporal coexistence of distinct and even opposing stress regimes, a pattern also recognized in previous studies, albeit at more local scales (e.g. Pérez-Flores et al., 2016). The most frequently observed regime corresponds to the one initially identified at the regional scale: a strike-slip regime with σ_1 and σ_3 orientated NE and NW, respectively. Additionally, a localized stress regime with a vertical σ_1 has been systematically observed in several large volcanoes, likely resulting from transient stress rotation driven by magma pressure (Pérez-Estay et al., 2023).

3. METHODS AND RESULTS

3.1. Long-term deformation: fault slip data from crustal faults, a harmonized new compilation.

Over the past 15 years, the quantity and quality of fault-slip data collected in the field, particularly in the volcanic arc region, have significantly improved, yielding new insights into Pliocene and younger slip partitioning and the regional and local strain/stress states (Sánchez et al., 2013; Pérez-Flores et al., 2016; Sielfeld et al., 2019a, b; Ruz-Ginouves et al., 2020; Mura et al., 2025). Figure 3 presents a summary of all the data collected from structural sites mapped by our research group since the early 1990s (see the Data and Resources chapter at the end of this manuscript for the complete dataset). We deliberately included only results from our group because the conceptual approach and field methodology have been applied consistently, using the same geological and structural criteria to define the geometry and kinematics of mesoscopic faults (see, for instance, Pérez-Flores et al., 2016). In the Discussion section these results are placed into a broader literature context.

Our compilation includes around 2,300 mesoscopic fault surfaces, for which we recorded the strike, dip, and rake of the striae. These faults affect Cretaceous to recent rock units, although only those that are clearly post-Miocene were considered in the analysis of current slip partitioning because the plate convergence vector, as stated earlier, has remained nearly constant in magnitude and direction over the past 20 Myr. Faults affecting Cretaceous and Paleogene rock units in the forearc are presented to account for earlier deformation patterns expected to differ from those of neotectonic activity.

Faults were identified and measured along the master and subsidiary faults of the LOFS, along NW- and WNW-striking transverse faults in the intra-arc, and at five sites in the forearc (Fig. 3). Fault displacement sense was determined by examining key features on the fault planes, including secondary fractures, mineral crystallization, and tension cracks, among other kinematic indicators (e.g., Petit, 1987). The orientations of the maximum shortening (P) and maximum stretching (T) instantaneous axes for each fault plane were obtained through FaultKin v.7.4.1 (Marrett and Allmendinger, 1990; Allmendinger et al., 2012), based on the fault plane's orientation and the resolved displacement vector (slickenline). The representative orientations of the P and T axes for a fault population were calculated under the assumption of small single displacements and a consistent deformation field, by assuming a statistical Bingham distribution. Non-clustered P- and/or T-axes suggest kinematic heterogeneity in faulting, which may be caused by factors such as triaxial deformation or reactivation of anisotropies. Neighboring sites with consistent P–T results were grouped to make the data easier to understand and visualize, obtaining 18 clusters (Fig. 3). In eight of these (Farellones, Maipo, Teniente, Teno, Maule, Lonquimay, Ranco, and Puyuhuapi), more than one solution was identified, resulting in two to four P–T axis stereoplots (Fig. 3). As we focus on deformation and slip partitioning rather than stress fields, we chose to present the data in a manner that reflects observations with minimal interpretation, consciously avoiding stress inversion programs. For the interested reader, stress field analyses conducted for the study area can be found in Arancibia et al. (1999), Cembrano and Lara (2009), Pérez-Flores et al. (2016), Sielfeld et al. (2019b), and Pérez-Estay et al. (2023), among others.

Overall, regional-scale analysis of the P-T axes from fault slip data in the volcanic arc indicates two primary maximum shortening axes: one oriented N60°E and the other trending ~E-W. In both cases, the minimum shortening axis is predominantly horizontal. When analyzed in greater detail, the following is recognized (Fig. 3):

(1) Sites in the forearc between 33° and 34° S were mapped in Cretaceous rock units (Colliguay), while those in Rapel and San Antonio affect Neogene sedimentary rocks. Although these sites exhibit a high dispersion in kinematic axis solutions, both P and T axes are predominantly subhorizontal, with roughly E-W shortening in clusters Colliguay and Rapel. North of 34° S, sites San Antonio, Farellones, and Maipo display a margin-parallel shortening. Sites at Farellones cut Miocene rock units, whereas those at Maipo affect Quaternary strata (Lavenu and Cembrano, 2008). Clusters Pelequén and Los Andes show a higher dispersion in the kinematic axis solutions, but a general NE-trending horizontal P-axis and a NW-trending subhorizontal T-axis. Faults at these sites affect Cretaceous to Miocene rock units.

(2) In the volcanic arc north of 34.5° S, a subhorizontal, roughly E–W shortening is also present, as documented at sites Farellones and Maipo. At these sites, extension axes are predominantly subhorizontal to horizontal, whereas at Teniente, just west of the volcanic arc, horizontal N–S shortening is documented. Faults at Teniente cut Pliocene rock units.

(3) Farther south, in the Main Cordillera at the Teno site (~35°S), the P-axis solution remains ~E–W, with both P and T subhorizontal. This solution is compatible with the dominant NE-dextral and NW-sinistral strike-slip faults

observed in the field. Most of these faults are no older than Oligocene or Miocene.

(4) At around 36° S, sites within the intra-arc area (Maule site) were mainly mapped in Oligocene to Pleistocene volcano-sedimentary rocks. Fault-slip analysis reveals three distinct orientations of the P-T axis. The first features a horizontal NE-trending P-axis that aligns with the regional ~N60°E maximum shortening direction. The second displays a horizontal P-axis rotated to N60°W. However, the most prevalent orientation is characterized by a nearly vertical P-axis and a N-S trending T-axis, compatible with E-W striking Pliocene–Pleistocene normal faults.

(5) In the forearc at 38° S (Esperanza site), faults that displace Quaternary sedimentary rocks (Lavenu and Cembrano, 1999) show a horizontal N–S trending P-axis with a near-vertical T-axis.

(6) Between 38° and 42° S, all clusters within the intra-arc domain exhibit a horizontal to slightly plunging NE-trending P-axis and a horizontal to slightly inclined NW to NNW-trending T-axis. Some individual sites at Lonquimay and Ralco show a slight clockwise rotation of both P- and T-axes towards E–W and N–S trends, respectively. The maximum age of the mapped faults is Miocene.

(7) Near the southern end of the study area (~44.5° S), the Puyuhuapi cluster represents faults affecting Miocene and Pliocene rock units. Fault-slip analysis indicates two main kinematic axis solutions: one with a horizontal-to-subhorizontal NE-trending P-axis and a horizontal-to-subhorizontal NW-trending T-axis, and another showing clockwise rotation of both P- and T-axes toward E-W and N-S, respectively.

3.2 Short-term deformation: integrated seismological data from crustal earthquakes from local networks

The availability of seismological data from crustal faults in the southern Andes has significantly increased both in quantity and quality over the past two decades (e.g., Lange et al., 2008; Mora et al., 2010; Legrand et al., 2011; Agurto et al., 2012; Sielfeld et al., 2019a). This has been possible thanks to the deployment of local networks focused on current deformation processes and stress state, particularly for the arc and forearc regions (e.g., Farías et al., 2011; Ammirati et al., 2019; Pearce et al., 2020; Pérez-Estay et al., 2020; Stanton-Yonge et al., 2025). These developments have also enabled the identification of seismogenic faults within known regional-scale fault systems and the potential discovery of unknown concealed faults. Previously, seismic data were mostly accessible only through the U.S. Geological Survey global seismological network, with a few exceptions noted in local studies (Barrientos and Acevedo, 1992).

We compiled focal mechanisms of seismic activity detected by temporary local networks in and next to the volcanic arc domain (Fig. 4), reported on previously published studies (Lange et al., 2008; Mora et al., 2010; Agurto et al., 2014; Ammirati et al., 2019; Sielfeld et al., 2019a; Pérez-Estay et al., 2020; Montenegro et al., 2021; Mura et al., 2025; Stanton-Yonge et al., 2025) to examine the current deformation processes occurring in the overriding plate. Due to variability in magnitudes, azimuthal gaps, and the number of observations at each source, all mechanisms were included, as each dataset comes from a previously validated and published study.

Figure 4d displays the distribution of P–T axes of focal mechanisms identified, along with the number of mechanisms per network. We selected three regions covered by one or more local networks to examine the spatial distribution of microseismicity and crustal faults: Maipo (Ammirati et al., 2019; Fig. 4A), Araucanía (Sielfeld et al., 2019; Montenegro et al., 2021) (Fig. 4B), and Aysén (Mora et al., 2010; Agurto et al., 2014; Pérez-Estay et al., 2020) (Fig. 4C). The seismicity detected by the local networks is shown as green dots and ranked by depth, along with a representative subset of focal mechanisms from each network (full focal mechanisms database available in the original references or in the Data and Resources chapter). A detailed discussion about seismicity rates in each region is beyond the scope of this work. Instead, the figures highlight the overall deformation pattern of the upper plate, as reflected in the orientations and distributions of the P and T axes.

The reported seismicity generally covers relatively short time windows (typically between 1 and 3 years of observation) and includes only events with Mw<5.0. Thus, it provides only a partial view of the ongoing processes and does not necessarily represent the activity of major faults. Nevertheless, this information is valuable because: (1) it allows spatial comparison between mapped faults and small earthquakes, and (2) the high density of local stations makes it possible to estimate focal mechanisms of small events that are not included in global catalogs. As our results focus on seismic network deployments within and around the volcanic arc domain, there is an inherent bias toward detecting higher seismicity rates in the arc than in the forearc. However, the global compilation presented in figure 2 partly compensates for this gap.

In figure 4, the current kinematics in the forearc and arc regions are evidenced by numerous shallow crustal earthquakes of relatively small magnitude. The orientations of P-T axes from focal mechanisms indicate a variety of fault kinematics. The main observations are:

(1) Strike-slip focal mechanism solutions primarily characterize the arc region between 34° and 47° S, with isolated normal events and even fewer reverse events (e.g., Chinn and Isacks, 1983; Lange et al., 2009; Sielfeld et al., 2019a; Pérez-Estay et al., 2020). This aligns with the global catalog results shown earlier (Fig. 2). Conversely, the coexistence of reverse and strike-slip focal mechanisms has been recorded only within the Main Cordillera between 33° and 34° S (e.g., Farías et al., 2006; Ammirati et al., 2019) (Fig. 4A). This transition from radial shortening observed north of 34° S (non-partitioned) to partitioned deformation south of 34° S, coincides with a marked increase in convergence obliquity south of 34° S, related to a significant change in trench orientation from nearly N-S to NNE.

(2) In the Maipo area (Fig. 4A), the P–T axes exhibit high dispersion, likely related to local stress perturbations around faults, but reverse kinematics predominate. The nodal plane covers a wide range of orientations, but nearly N–S and E–W trending P-axis solutions are prevalent. Strike-slip kinematics are consistent with predominant E–W shortening.

(3) Farther south, in the Araucanía and Aysén regions (Fig. 4B, C), margin-parallel, strike-slip kinematics predominate, with NE-trending shortening consistent with either dextral slip in subvertical N-to-NNE striking faults, or sinistral slip in WNW-striking faults. Local observations of extensional

kinematics are detected, with nodal fault planes consistent with ENE-striking normal faults.

(4) Strike-slip deformation in the arc domain, coherent with ~N–S striking mapped dextral faults, suggests a northward motion of the forearc sliver, accompanied by margin-parallel shortening at its leading edge, i.e., a buttress effect (Beck et al., 1993; Lavenu and Cembrano, 1999; Farías et al., 2006).

4. DISCUSSION

4.1. Exploring the role of margin-parallel versus transverse faults on slip partitioning

Subtle but sharp along-strike variations in the continental margin trend affect the magnitude of the strike-slip component derived from the oblique convergence vector. (e.g., Stanton-Yonge et al., 2016; Fig. 2). In the end-member scenario of complete slip partitioning (Fig. 1A), where slip at the plate interface exclusively accommodates the margin-normal component of convergence, the total margin-parallel component that should be accommodated by intra-arc faulting is estimated to be ~35 mm/year between 33° and 38° S and ~24 mm/year between 38° and 47° S.

Under a complete partitioning scenario, the slip vectors of subduction earthquakes would be oriented orthogonal to the margin (Beck, 1991; McCaffrey, 1992). However, Stanton-Yonge et al. (2016) obtained an average slip direction of N89°E by analyzing 20 subduction earthquakes for the 33-39° S region. This indicates that slip at the plate interface accommodates only part of the oblique convergence, suggesting partial partitioning in this segment (Fig. 1B). The difference between the convergence vector and the thrust earthquake slip vectors leads to a residual slip vector of 13.5 mm/year of margin-parallel displacement, which should be

accommodated in the upper plate between 33° and 38° S, and 12.1 mm/year between 38° and 47° S (Fig. 2).

Applying the same analysis to a more recent subduction earthquake that occurred at 43° S (December 2016; Mw 7.6), the slip vector has a trend of N93°E, which is close to the margin-orthogonal orientation (~N100°E). This indicates a more complete partitioning toward the southern end of the study area and, consequently, a larger margin-parallel slip component that must be accommodated within the upper plate (~17 mm/year).

Fault slip estimates at the northern end of the LOFS, whether seismic or aseismic, can reach as high as 18 mm/year (Astudillo-Sotomayor et al., 2021). However, this finding poses a potential inconsistency: even if the single fault examined by Astudillo-Sotomayor et al. (2021) accounted for all margin-parallel slip vectors, the slip rate should be only ~13 mm/year, which is the expected end-member of partial partitioning (Stanton-Yonge et al., 2016). Furthermore, because the LOFS consists of multiple subparallel strands, the overall potential slip should be accommodated across multiple faults. It is also important to note that *in situ* block rotation and permanent distributed strain across the upper plate have been documented, deformation components that also contribute to accommodating the oblique convergence at the plate margin (García et al., 1988; Rojas et al., 1994; Cembrano et al., 2002; Hernández et al., 2014, 2016). A plausible explanation for the unusually high slip rate observed by Astudillo-Sotomayor et al. (2021) is that the northward displacement of the forearc sliver, driven by the Chile Ridge subduction at 46° S, may significantly amplify dextral strike-slip along margin-parallel faults (e.g., Forsythe and Nelson, 1985; Cande and Leslie, 1986; Cembrano et al., 2002). On the other

526 hand, at the southernmost segment of the LOFS (~46° S), De Pascale et al. (2021)
527 suggested a Quaternary dextral slip rate of 11 to 24 mm/year based on displaced
528 glacial landforms, calculations that however should be interpreted with caution, as
529 the dates of the glacial landforms are not sufficiently well-constrained.

530 Regarding the role of margin-parallel versus margin-oblique faults in slip partitioning,
531 transverse faults can effectively accommodate part of the margin-orthogonal
532 component of oblique convergence across the submerged forearc, arc, and back-arc
533 regions (e.g., Sielfeld et al. 2019b). This observation supports the concept of
534 kinematic partitioning of overall transpressional deformation at all scales, from
535 regional to local (Fig. 1C). Transverse faults may also accommodate different long-
536 and short-term, along-strike shortening when acting as transfer faults (e.g.,
537 Arriagada et al. 2000), where faults can switch displacement sense at various time
538 scales.

539 **4.2. The seismic versus aseismic nature of long-term fault slip**

540 While there is a significant spatial correlation between long-term faulting and current
541 crustal earthquakes, the extent to which slip is accommodated through seismic and
542 aseismic processes remains elusive. This uncertainty has important implications for
543 our understanding of fault mechanics in the upper crust and for estimates of a fault's
544 seismic potential.

545 In the study area, mesoscopic fault surfaces with striae (slickensides) typically show
546 one or more of the following features: ridge-and-groove striae, mineral fibers, mineral
547 precipitation behind fault steps, breccia patches, and gouge (Fig. 5). The widespread
548 presence of mineral fibers behind fault steps rather than bladed calcite (believed to
549 be representative of seismic slip), along with the apparent lack of pseudotachylytes

(friction-induced melts), suggests that most of the mapped mesoscopic faults represent aseismic slip.

The debate surrounding whether fault surfaces and their kinematic indicators, as observed in the field, represent seismic slip or slow slip has persisted for decades (Rowe and Griffith, 2015, and references therein). One interpretation of aseismic creep involves mineral fibers and the pressure solution process. Pressure solution is an effective mechanism that dissolves asperities that hinder fault slip and promotes the growth of mineral fibers within fault slip zones (e.g., Gratier and Gamond, 1990; Gratier et al., 2011). It includes successive stages: dissolution, transfer, and deposition, indicating a slow displacement that is not relevant to the dynamic movement of large earthquakes (e.g., Rutter, 1983). However, recent studies suggest that creep processes may not relieve tectonic stress sufficiently to prevent earthquake rupture, and some have even proposed that a creeping fault could still produce large-magnitude earthquakes (e.g., Noda and Lapusta, 2013; Chen and Bürgmann, 2017).

The lack of evidence for seismic slip in an exhumed fault zone does not exclude a seismogenic history. For example, pseudotachylytes are among the most reliable indicators of paleo-seismic slip (Rowe and Griffith, 2015). Experimental research indicates that they can form after only millimeters of seismic slip (e.g., Niemeijer et al., 2011), suggesting that they should be common in seismogenic faults. Pseudotachylytes are, however, rarely reported in the literature, possibly due to the difficulty in identifying them (e.g., Kirkpatrick and Rowe, 2013) and their rapid removal from the geological record through hydrothermal alteration (e.g., Fondriest et al., 2020). To our knowledge, with very local exceptions (see bladed calcite in

figure 5D), no conclusive seismic markers of any type have been documented along the exhumed outcrops associated with the LOFS. This lack of field evidence, however, does not preclude the LOFS from being seismogenic. In fact, the historic seismicity linked to this fault (Fig. 2) provides clear evidence of its current seismogenic nature, even though seismicity at the LOFS appears scattered and relatively infrequent for a fault that likely accommodates long-term slip rates of up to 20 mm/yr. The apparent mismatch between the fault's activity and its estimated long-term slip rates, combined with evidence in favor of paleo-aseismic slip, suggests that part of the slip may occur without earthquakes (e.g., Astudillo et al. 2023). A thorough characterization and quantification of the division between seismic and aseismic slip along the LOFS is beyond the scope of this study and would require detailed, long-term geodetic measurements.

4.3. The role of hot fluids in intra-arc brittle deformation

Records of crustal seismicity show more concentrated, intense activity in the intra-arc domain than in the adjacent forearc and back-arc regions (e.g., Weller, 2012). Additionally, whereas crustal seismicity in these latter two regions can reach depths of ~30 km, the typical depth of the crustal seismogenic zone in the intra-arc is ~10 km. The inverse relationship between brittle crustal thickness and the geothermal gradient supports the idea that active magmatic regions experience higher strain rates, promoting feedback between fracturing, increased permeability, and fluid flow (e.g., Rowland and Simmons, 2012). Rock strength decreases when fluids are present within the rock-mass porosity, leading to greater damage under a given far-field differential stress (Lockner, 1995). Conversely, the absence of fluids results in less strain under the same stress regime. Therefore, the combined effect of a thin,

brittle volume containing fluid will cause concentrated damage and larger slip magnitudes than those otherwise predicted from mechanical strain partitioning alone. Although no quantitative studies have yet shown the exact amount of slip contributed by these combined factors, we expect it to be on the order of a few millimeters per year.

4.4. Significance of long- and short-term kinematics in the along- and across-strike segmentation of the Southern Andes

Our new and revised compilation of fault slip data, along with crustal earthquake focal mechanisms from global and local networks, provides an improved understanding of the nature of slip partitioning between 33° and 47° S. Four main segments are proposed (Fig. 6):

1. 33-34° S, characterized by a very small oblique convergence angle and no margin-parallel intra-arc faulting. E-W shortening is accommodated by ENE dextral and WNW sinistral strike-slip faults within the arc domain, and by margin-parallel reverse faults in the back-arc (e.g., Ammirati et al., 2022). Deformation in this segment is also characterized by several local Quaternary faults in the forearc and arc regions, consistent with ~N–S shortening (Lavenu and Cembrano, 2008, 2009). These faults are kinematically consistent with present-day earthquake focal mechanisms (Figs. 2 and 4). The coexistence of ~E–W and ~N–S shortening in this segment can be explained by a radial compression strain/stress field, particularly along the WNW boundary zone (here named the Maipo deformation zone) between segments 1 and 2. The Maipo deformation zone occurs at the Maipo Orocline, and coincides with a regional WNW magnetic anomaly and surface faults (Wall et al., 1996; Yáñez

et al., 1998, 2024; Arriagada et al., 2013; Piquer et al., 2021). Radial compression at the southern boundary of this segment was suggested by Allmendinger et al. (2006) based on independent GPS and geological data. The Maipo boundary also marks a sharp transition in rock exhumation and an elevation drop of about 2 km in the Main Cordillera (Figs. 2 and 6), also coinciding with a key geological discontinuity where the Frontal Cordillera ends (e.g., Ramos et al., 1986).

2. 34-37° S, characterized by a more pronounced oblique convergence, partitioned into margin-parallel dextral faults and margin-oblique transverse faults. The first ones are mostly blind, i.e., documented almost exclusively by earthquake focal mechanisms, yet with a few exceptions (e.g., the El Melado Fault; Cardona et al., 2018; Sielfeld et al., 2019b). At around 35.5° S, a set of ENE-striking dextral transtensional faults is spatially associated with a marked shift in the location of the present-day volcanic arc front (e.g., Sielfeld et al., 2019b; Ruz-Ginouves et al., 2020). In this segment, a portion of the margin-orthogonal shortening component is accommodated by WNW sinistral transpressional faults and NE dextral faults, of which the former appears to be seismically active (Stanton-Yonge et al., 2016, 2025; Vigide et al., 2025). The boundary between segments 2 and 3 corresponds to a set of NW-striking faults, of which the most prominent is the Lanalhue Fault (e.g., Melnick et al., 2009). This boundary also coincides with significant latitudinal changes in exhumation levels, especially in the forearc region. We propose that this boundary is a crustal-scale, steeply dipping, south-verging reverse fault, in accordance with the work by Melnick et al. (2009).

3. 37-41°S. This segment features a well-documented margin-parallel slip component, accommodated by the LOFS and by seismically active NW and NE strike-slip faults. The emerged forearc region is characterized by margin-parallel shortening active since at least the late Pliocene epoch, as suggested by fault slip data and current focal mechanisms. The ~N–S shortening is probably a consequence of a buttress effect acting on the leading edge of the northward-moving forearc sliver (e.g., Beck et al., 1993; Melnick et al., 2009; Astudillo et al., 2023). The southern boundary of this segment is marked by the WNW-striking Chacao Fault System north of Chiloé Island. Surface geology reveals, in this southern end, a contrast in exhumation levels, particularly along the volcanic arc, where mylonites to the north give way to brittle faults to the south (e.g., Cembrano et al. 2000).

The LOFS ends as an extensional imbricate fan (horsetail structure) at around 38° S and connects with the Antiñir-Copahue Fault System in the back-arc (Folguera et al., 2004; Melnick et al., 2006; Pérez-Flores et al., 2016). Regardless of how dextral strike-slip motion is accommodated at the northern end of the LOFS, the northward movement of the forearc sliver should decrease to nearly zero at the same latitude. This is because fault displacement should be maximum at the central or trailing segments of any strike-slip fault, naturally tapering off approaching their leading edge, especially when they are buttressed (e.g., Beck et al. 1993). This creates a latitudinal displacement gradient, resulting in margin-parallel shortening of the forearc accompanied by counterclockwise tectonic rotation (e.g., Hernández-Moreno, 2014, 2016). Margin-parallel shortening has also been observed in the forearc of northern Chile (González et al., 2008; Allmendinger and

González, 2010), where conspicuous E–W faults are currently active. A similar pattern of margin-parallel shortening and block rotation has been found in the forearc of Cascadia (e.g., Johnson et al. 2004). In Cascadia, as well as in the Southern Andes, roughly E–W margin-normal compression dominates the forearc region near the trench, where the plates appear to be locked. In contrast, when slow slip and tectonic tremors dominate the subduction interface, and the plates are less strongly coupled, the forearc begins to accommodate the margin-parallel shortening through strike-slip and thrust at transverse crustal faults (e.g., Balfour et al., 2011).

4. 41-47° S. This segment accommodates most of the upper plate deformation through a transtensional strike-slip duplex composed of two right-stepping margin-parallel dextral strike-slip faults joined by NE-trending normal and dextral-normal faults (Cembrano et al., 1996). Fault-slip data and earthquake focal mechanisms are internally consistent with the long-term kinematics of the LOFS (Arancibia et al., 1999; Lavenu and Cembrano, 1999; Cembrano et al., 2002; Pérez-Estay et al., 2020). The northward, margin-parallel motion of the forearc sliver is strongly supported by geological, geodetic, paleomagnetic, and seismological data (Beck et al., 1993; Rojas et al., 1994; Cembrano et al., 2000; Wang et al., 2007; Melnick et al., 2009; Moreno et al., 2016; Sielfeld et al., 2019a).

Tectonic boundaries between segments 1-2 and 2-3 are interpreted in this work as major, deep-seated south-verging reverse faults. The boundary between segments 3-4 is also a crustal-scale fault, although there is no clear evidence of vergence. Based on geological mapping and geophysical evidence, Yáñez et al. (2024) identified these features as first-order, long-lived tectonic structures, likely active

since at least the Permo-Triassic. During the Neogene-Quaternary, these faults have influenced the location of volcanic alignments and ore deposits in the arc domain (e.g., Lara et al., 2004; Cembrano and Lara, 2009; Piquer et al., 2015).

4.5. Implications for seismic hazard

Local paleo-seismological, geophysical, and morphological studies focused on specific fault strands have provided estimates of their geometry, kinematics, and recurrence intervals for the studied area Notable examples include the works of Vargas et al. (2014) and Yáñez et al. (2020) on the west-verging, reverse San Ramon Fault in the Andean foothills of Santiago (33.5° S), with slip rates estimated between 0.3-0.5 mm/year. At around 36° S, Vega-Ruiz et al. (2025) investigated Quaternary deformation along the western margin of the Main Cordillera driven by west-verging reverse faults, obtaining slip rates of up to 0.58 mm/year and estimated a maximum Mw of 7.0. Further south, in the LOFS domain, morphotectonic analyses of well-exposed master and splay faults have revealed slip rates of 10-22 mm/year (Astudillo et al., 2018, 2021, 2023; De Pascale et al. 2021), significantly higher when compared to estimates in the north. However, smaller slip-rate values are obtained from numerical modeling: 1 to 7 mm/year for the margin-parallel LOFS, ~1 mm/year for the Andean transverse faults, and 5-10 mm/year along the southern master faults of the LOFS (e.g., Stanton-Yonge et al., 2016; Iturrieta et al., 2017).

While these studies have greatly enhanced our understanding of seismic hazards in Chile, there has been a lack of systematic efforts to contextualize the fault systems within a broader tectonic framework. Specifically, there has been insufficient discussion of their role in plate margin partitioning and of the interplay between the seismic and aseismic components of the reported fault displacements. Moreover,

long-term evidence of fault slip for many of these potentially hazardous faults has not been critically integrated into the discussion surrounding the primary geological processes involved, complicating comparisons with short-term deformation observations. However, compilations focused on the nature and spatial distribution of Quaternary crustal faults in the studied region (e.g., Lavenu et al., 2000; Santibañez et al., 2019; Maldonado et al., 2021) are available, while Costa et al. (2020) presented a compilation of Quaternary faults for South America and provided an estimation of the regional-scale seismic hazard.

In terms of seismic hazard, our synthesis of crustal seismicity and long-term fault-slip data suggests the following:

1. Aseismic slip should be considered when interpreting data from morphotectonic analyses and fault separation of markers in potentially seismogenic faults (e.g., LOFS). In fact, Astudillo et al. (2023) observed a discrepancy between their estimated slip rates and the recurrence times of historical earthquakes in the LOFS, with aseismic slip required to reconcile the two. This observation is consistent with long-term evidence of displacement in mesoscopic faults within the same fault systems where Holocene fault slip estimates have been made, indicating that these faults exhibit a significant amount of aseismic slip, as demonstrated by the presence of slickenfibers on fault surfaces and shear bands, which are commonly used as kinematic indicators (e.g., Pérez-Flores et al. 2016). Evidence for seismic slip in fossil faults is often elusive (e.g., Rowe and Griffith, 2015), and only specific microstructures indicate dynamic rupturing. The primary implication of the above points is that many morphotectonic and paleo-seismological studies may significantly

overestimate seismic fault-slip rates, thereby exaggerating deterministic estimates of earthquake magnitudes (e.g., Burgmann, 2018).

2. The tectonic transitions between the proposed segments identified in this study are likely to play (and have played) a crucial role in the seismo-tectonic segmentation of the margin. For instance, Yáñez et al. (2024) suggested that trans-lithospheric faults have acted as regions of weak coupling, functioning as long-term, geologically controlled seismic barriers. The release of fluids from the Wadati-Benioff zone could be the driving force behind this creep-like mechanism. Ample evidence of reverse faulting in these boundary zones is a key factor in understanding these potential seismic barriers.

3. In probabilistic seismic hazard analysis (PSHA; e.g., Gerstenberger et al., 2020), the contribution of crustal faults should be evaluated alongside the dominant subduction interface hazard. In addition, because crustal sources are typically shallow and near the sites of analysis, they can locally elevate seismic hazard within a narrow spatial range. In the near-fault region, the long-return-period tail of the hazard curve can be controlled by the fault itself, even when its occurrence rates are low (e.g., Youngs and Coppersmith, 1985; Baker, 2013). In our compiled instrumental catalog, the maximum documented magnitudes for intra-arc events are Mw 6.5 in the north and Mw 6.2 in the south. Traditional PSHA studies complement seismicity observations by constraining the maximum magnitude and the magnitude-frequency distribution using mapped fault geometries and slip rates (e.g., Gerstenberger et al., 2020). Despite notable efforts to characterize faults in Chile (e.g., Santibáñez et al., 2019; Maldonado et al., 2021), further work is needed to determine slip rates across all seismogenic faults in a harmonized, systematic manner (e.g., Seebeck et al., 2023; Basili et

al., 2024). Future PSHA would certainly benefit from more accurate estimates on interseismic slip rates from geodesic and remote sensing data (e.g., Chaussard et al., 2016), along with physics-based rupture models, to explore the seismic potential of crustal faults, including the contribution of slow slip to the earthquake cycle (e.g., Bürgmann, 2018). For instance, dense, near-fault Global Navigation Satellite System surveys could geodetically constrain interseismic strain, steady creep, and/or transient slow-slip events (e.g., Rousset, 2019), thereby better constraining the seismic slip deficit relevant for hazard assessment.

5. CONCLUSIONS

The combination of new and unpublished fault-slip data, and of regional and local crustal seismicity, enables an updated understanding of the geometry and kinematics of slip partitioning along and across the South American plate boundary between 33° and 47° S. This partitioning proves to be much more complex than previously thought, with implications for plate-margin tectonics, the spatial and temporal distribution of fault slip, and interactions with other processes such as active faulting and volcanism.

Slight variations in the along-strike orientation of the continental margin influence different stress and strain distributions. Radial shortening (constriction) dominates the Maipo Orocline region between 33° and 34° S, as margin-orthogonal and margin-parallel shortening spatially coincide in a zone where there is a transition from non-partitioned to partitioned deformation. Another important change occurs at around 37° S, where the strike-slip component of the convergence vector is reduced, and the transcurrent margin-parallel slip is absorbed by a major, continuous intra-arc fault system, the LOFS, between 37° and 46° S. Region-wide, the predominantly E–W

shortening documented in the submarine forearc contrasts with the margin-parallel shortening observed from seismicity and fault slip data along the emerged forearc region. In the arc domain, a combination of E–W shortening and NE–SW shortening, the latter accommodated by a mostly hidden dextral fault between 34° and 37° S, is then replaced to the south by a continuous surface expression of dextral faulting and transverse, seismically active NE and NW dextral and sinistral faults.

The forearc sliver between 33° and 47° S is divided into four main blocks, separated by prominent WNW- to NW-striking fault zones that may or may not extend into the volcanic arc region. At the Maipo Orocline zone, a WNW transverse deformation zone/fault places deeper crustal levels in the north over shallower levels in the south, indicating a predominantly south-verging reverse fault or deformation zone. Surface faults, such as Melipilla, Piuquencillo, and Pichilemu, are believed to be surface expressions of this WNW deformation boundary. Farther south, at the Arauco Peninsula region, where the continental margin shifts from a NNE to a ~N-S orientation, another major NW-striking boundary separates Silurian-to-Permian metamorphic rocks and intrusives to the north from mostly Paleozoic metamorphic rocks to the south. As noted in previous works, this boundary is represented at the surface by the NW-striking, south-verging Lanalhue reverse fault, which tends to fade toward the volcanic arc. The fourth and last crustal block lies south of the WNW-striking, mostly reverse, south-verging Chacao Fault, and is dominated by the LOFS strike-slip duplex as the main tectonic element, which mostly accommodates dextral strike-slip deformation.

Finally, in the LOFS, evidence for mostly slow slip (observed on exhumed striated fault surfaces from where instantaneous shortening and extension axes were

derived) challenges the idea that these mesoscopic faults are fossil earthquake sites and raises questions about whether seismic events are always the source of the morphological and stratigraphic evidence of slip. It is therefore very likely that calculated slip rates overestimate the seismic slip budget, thereby affecting seismic hazard assessments.

6. Acknowledgements

The senior authors of this paper would like to warmly thank Francisco Hervé for inspiring us in our early stages as independent researchers. This paper is dedicated to him. Pancho introduced us to the Liquiñe-Ofqui Fault System in the late 1980s, and from then on, it has captivated our interest and encouraged us to go further than previous generations, along with many bright students, our junior coauthors, who are now moving the frontiers of science. Numerous Fondecyt projects have generously supported most of the research shown in this paper over the last few decades. The first of these, headed by Pancho, was also supported by later projects shared with Francisco Munizaga, Luis Lara, Hugo Moreno, Leopoldo López-Escobar, among several others. The Andean Geothermal Center of Excellence, led by Diego Morata and beginning in 2001, significantly advanced work in key areas of the Southern Andes. We sincerely thank our friends Luis Lara and Gabriel González for the many insightful discussions we have had over the years on the topics covered in this paper. Many M.Sc. and Ph.D. ANID scholarships provided crucial funding for the junior co-authors to develop innovative ideas on various topics related to slip partitioning, using a combination of traditional geological and geophysical techniques and cutting-edge numerical modeling.

Alain Lavenu's stay in Chile was funded by ORSTOM and later by IRD for several years. This marked the start of research on the kinematic analysis of fault surfaces and how this knowledge was passed down through generations in Chile.

Constanza Rojas and José Cembrano would like to thank Prof. Myrl Beck from Western Washington University, who introduced them to the concept of slip partitioning and paleomagnetism at convergent margins in the early 1990s. He is no longer with us, but his passion for tectonic processes lives on in our hearts.

The manuscript was greatly improved thanks to the helpful comments from reviewers Keith Klepeis and Carolina Canora. We are especially grateful to Guest Editor Robert Pankhurst for his patient review, thoughtful editing, and careful handling of the manuscript. Lastly, we sincerely thank Mauricio Calderón for encouraging us to submit our work to this special issue.

7. Data and Resources

The GCMT (https://www.globalcmt.org/; Ekström et al., 2012) and ANSS-ComCat (https://earthquake.usgs.gov/; U.S. Geological Survey, 2017) catalogs were last accessed on August 1, 2025. Local-network hypocenters and focal mechanisms were compiled from the published studies cited in the text. Slab geometry was obtained from the Slab2 model (Hayes et al., 2018). Data processing and catalog merging/classification were performed in Python, with the assistance of the obspy (Beyreuther et al., 2010), pycsep (Savran et al., 2022), mplstereonet (https://pypi.org/project/mplstereonet/), and FMC (Alvarez-Gomez, 2019) packages. Fault-slip kinematic summaries and stereonets were generated with FaultKin (Allmendinger et al., 2012). The final maps were prepared in QGIS (https://www.qgis.org). All collected catalogs, fault kinematic measurements, and the

derived and processed datasets are archived in the accompanying Zenodo repository: https://doi.org/10.5281/zenodo.17296704.

References

Agurto, H.; Rietbrock, A.; Barrientos, S.; Bataille, K.; Legrand, D. 2012. Seismotectonic structure of the Aysén Region, Southern Chile, inferred from the 2007 Mw=6.2 Aysén earthquake sequence. Geophysical Journal International 190: 116-130. https://doi.org/10.1111/j.1365-246X.2012.05507.x

Agurto-Detzel, H.; Rietbrock, A.; Bataille, K.; Miller, M.; Iwamori, H.; Priestley, K. 2014. Seismicity distribution in the vicinity of the Chile Triple Junction, Aysén Region, southern Chile. Journal of South American Earth Sciences 51: 1-11. https://doi.org/10.1016/j.jsames.2013.12.011

Allmendinger, R.; Yáñez, G.; Cembrano, J. 2006. Instantaneous deformation associated with flat subduction: Insights from GPS strain rates and numerical modelling. In Congreso Geológico Chileno, No. 11, Actas 1: 367–370. Antofagasta, Chile.

Allmendinger, R.W.; González, G. 2010. Invited review paper: Neogene to Quaternary tectonics of the coastal Cordillera, northern Chile. Tectonophysics 495 (1-2): 93-110. https://doi.org/10.1016/j.tecto.2009.04.019

Allmendinger, R.W.; Cardozo, N.C.; Fisher, D. 2012. Structural Geology Algorithms: Vectors & Tensors. Cambridge University Press. 289.

Álvarez-Gómez, J. A. 2019. FMC—Earthquake focal mechanisms data management, cluster and classification. SoftwareX, 9, 299-307. https://doi.org/10.1016/j.softx.2019.03.008

Ammirati, J-B.; Vargas, G.; Rebolledo, S.; Abrahami, R.; Potin, B; Leyton, F.; Ruiz, S. 2019. The crustal seismicity of the Western Andean Thrust (Central Chile, 33º-34ºS): implications for regional tectonics and seismic hazard in the Santiago area. Bulletin of the Seismological Society of America 109 (5): 1985-1999. https://doi.org/10.1785/0120190082

Ammirati, J-B.; Villaseñor, A.; Chevrot, S.; Easton, G.; Lehujeur, M.; Ruiz, S.; Flores, M.C. 2022. Automated earthquake detection and local travel time tomography in the South-Central Andes (32-35ºS): Implications for regional tectonics. Journal of Geophysical Research: Solid Earth 127: e2022JB024097. https://doi.org/10.1029/2022JB024097

Angermann, D.; Klotz, J.; Reigber, C. 1999. Space-geodetic estimation of the Nazca-South America Euler vector. Earth and Planetary Sciences 171 (3): 329-334. https://doi.org/10.1016/S0012-821X(99)00173-9

Arancibia, G.; Cembrano, J.; Lavenu, A. 1999. Transpresión dextral y partición de la deformación en la Zona de Falla Liquiñe-Ofqui, Aisén, Chile (44-45ºS). Revista Geológica de Chile 26 (1): 3-22. http://dx.doi.org/10.4067/S0716-02081999000100001

Aron, F.; Allmendinger, R.W.; Cembrano, J.; González, G.; Yáñez, G. 2013. Permanent fore-arc extension and seismic segmentation: Insights from the 2010 Maule earthquake, Chile. Journal of Geophysical Research: Solid Earth 118: 724-739. https://doi.org/10.1029/2012JB009339

Arriagada, C.; Roperch, P.; Mpodozis, C. 2000. Clockwise block rotations along the eastern border of the Cordillera de Domeyko, Northern Chile (22º45'-23º30' S). Tectonophysics 326 (1-2): 153-171. https://doi.org/10.1016/S0040-1951(00)00151-7

Arriagada, C., Ferrando, R., Córdova, L., Morata, D., & Roperch, P. (2013). The Maipo Orocline: A first scale structural feature in the Miocene to Recent geodynamic evolution in the central Chilean Andes. Andean geology, 40(3), 419-437. http://dx.doi.org/10.5027/andgeoV40n3-a02

Astudillo, L.; Cortés-Aranda, J.; Melnick, D.; Tassara, A. 2018. Holocene deformation along the Liquiñe–Ofqui Fault Zone, southern Chile: Field observations and geomorphic analysis. In International INQUA Meeting on Paleoseismology, Active Tectonics and Archeoseismology (PATA), No. 9. Possidi, Greece.

Astudillo-Sotomayor, L.; Jara-Muñoz, J.; Melnick, D.; Cortés-Aranda, J.; Tassara, A.; Strecker, M.R. 2021. Fast Holocene slip and localized strain along the Liquiñe-Ofqui strike-slip fault system, Chile. Scientific Reports 11. https://doi.org/10.1038/s41598-021-85036-5

Astudillo-Sotomayor, L.; Cortés-Aranda, J.; Melnick, D.; Jara-Muñoz, J.; Cabello, C.; Perucca, L.; Tassara, A.; Pérez-Peña, J. V.; León-Ibáñez, P. 2023. Neotectonic faults in the Southern Chile intra-arc (38ºS-40.5ºS): Insights about their seismic potential and the link with the megathrust earthquake cycle. Tectonophysics 846, 229675. https://doi.org/10.1016/j.tecto.2022.229675

Baker, J. W. 2013. Probabilistic seismic hazard analysis. White Paper Version 2.0.1: 79.

Balfour, N.J.; Cassidy, J.F.; Dosso, S.E.; Mazzotti, S. 2011. Mapping crustal stress and strain in southwest British Columbia. Journal of Geophysical Research: Solid Earth 116 (B3): 1-11. https://doi.org/10.1029/2010JB008003

Barrientos, S.E.; Acevedo-Aránguiz, P.S.; 1992. Seismological aspects of the 1988-1989 Lonquimay (Chile) volcanic eruption. Journal of Volcanology and Geothermal Research 53: 73-87. https://doi.org/10.1016/0377-0273(92)90075-o

Basili, R.; Danciu, L.; Beauval, C.; Sesetyan, K.; Pires Vilanova, S.; Adamia, S.; Arroucau, P.; Atanackov, J.; Baize, S.; Canora, C.; Caputo, R.; Cosimo Carafa, M.M.; Cushing, E.M.; Custódio, S.; Demircioglu Tumsa, M.B.; Duarte, J.C.; Ganas, A.; García-Mayordomo, J.; Gómez de la Peña, J.; Gràcia, E.; Jamsek Rupnik, P.; Jomard, H.; Kastelic, V.; Maesano, F.E.; Martín-Banda, R.; Martínez-Loriente, S.; Neres, M.; Perea, H.; Sket Motnikar, B.; Tiberti, M.M.; Tsereteli, N.; Tsironi, V.; Vallone, R.; Vanneste, K.; Zupancic, P.; Giardini, D. 2024. The European fault-source model 2020 (EFSM20): Geologic input data for the European Seismic Hazard Model 2020. Natural Hazards and Earth System Sciences 24 (11): 3945-3976. https://doi.org/10.5194/nhess-24-3945-2024

Beck Jr., M.E. 1991. Coastwise transport considered: Lateral displacements in oblique subduction zones, and tectonic consequences. Physics of the Earth and Planetary Interiors 68: 1-8.

944 Beck Jr., M.E.; Rojas, C.; Cembrano, J. 1993. On the nature of buttressing in margin-parallel
945 strike-slip fault systems. Geology 21 (8): 755-758.

946 Beyreuther, M.; Barsch, R.; Krischer, L.; Megies, T.; Behr, Y.,; Wassermann, J. 2010.
947 ObsPy: A Python toolbox for seismology. *Seismological Research Letters, 81*(3): 530-
948 533. https://doi.org/10.1785/gssrl.81.3.530

949 Bravo, F.; Koch, P.; Riquelme, S.; Fuentes, M.; Campos, J. 2019. Slip distribution of the
950 1985 Valparaíso earthquake constrained with seismic and deformation data.
951 Seismological Research Letters, 90 (5): 1792-1800. https://doi.org/10.1785/0220180396

952 Bürgmann, R. 2018. The geophysics, geology and mechanics of slow fault slip. Earth and
953 Planetary Science Letters 495 (1): 112-134. https://doi.org/10.1016/j.epsl.2018.04.062

954 Cande, S.C.; Leslie, R.B. 1986. Late Cenozoic tectonics of the Southern Chile Trench.
955 Journal of Geophysical Research: Solid Earth 91 (B1): 471-496.
956 https://doi.org/10.1029/JB091iB01p00471

957 Canora, C.; Martínez-Díaz, J.; Villamor, P.; Staller, A.; Berryman, K.; Álvarez-Gómez, J.A.;
958 Capote, R.; Diaz, M. 2014. Structural evolution of the El Salvador Fault Zone: An evolving
959 fault system within a volcanic arc. Journal of Iberian Geology 40 (3): 471-488.
960 https://doi.org/10.5209/rev_JIGE.2014.v40.n3.43559

961 Cardona, C.; Tassara, A.; Gil-Cruz, F.; Lara, L.; Morales, S.; Kohler, P.; Franco, L. 2018.
962 Crustal seismicity associated to rapid surface uplift at Laguna del Maule Volcanic
963 Complex, Southern Volcanic Zone of the Andes. Journal of Volcanology and Geothermal
964 Research 353: 83-94. https://doi.org/10.1016/j.jvolgeores.2018.01.009

965 Cembrano, J.; Hervé, F.; Lavenu, A. 1996. The Liquiñe Ofqui fault zone: a long-lived intra-
966 arc fault system in southern Chile. Tectonophysics 259 (1-3): 55-66.
967 https://doi.org/10.1016/0040-1951(95)00066-6

968 Cembrano J.; Schermer, E.; Lavenu, A.; Sanhueza, A. 2000. Contrasting nature of
969 deformation along an intra-arc shear zone, the Liquiñe-Ofqui fault zone, southern Chilean
970 Andes. Tectonophysics 319 (2): 129-149. https://doi.org/10.1016/S0040-1951(99)00321-2

971 Cembrano, J.; Lavenu, A.; Reynolds, P.; Arancibia, G.; López, G.; Sanhueza, A. 2002. Late
972 Cenozoic transpressional ductile deformation north of the Nazca-South America-
973 Antarctica triple junction. Tectonophysics 354 (3-4): 289-314.
974 https://doi.org/10.1016/S0040-1951(02)00388-8

975 Cembrano, J.; Lara, L. 2009. The link between volcanism and tectonics in the southern
976 volcanic zone of the Chilean Andes: A review. Tectonophysics 471: 96-113.
977 https://doi.org/10.1016/j.tecto.2009.02.038

978 Charrier, R.; Baeza, O.; Elgueta, S.; Flynn, J.J.; Gans, P.; Mahlburg Kay, S. ; Muñoz, N. ;
979 Wyss, A.R. ; Zurita, E. 2002. Evidence for Cenozoic extensional basin development and
980 tectonic inversion south of the flat-slab segment, southern Central Andes, Chile (33ºS-
981 36ºS.L.). Journal of South American Earth Sciences 15 (1): 117-139.
982 https://doi.org/10.1016/S0895-9811(02)00009-3

983 Chaussard, E.; Bürgmann, R.; Fattahi, H.; Johnson, C.W.; Nadeau, R.M. 2016. Potential and
984 limits of InSAR to characterize interseismic deformation independently of GPS data:
985 Application to the southern San Andreas Fault system. Geochemistry, Geophysics,
986 Geosystems 17 (3): 1214-1229. https://doi.org/10.1002/2015GC006246

987 Chen, K.H.; Bürgmann, R. 2017. Creeping faults: good news, bad news? Reviews of
988 Geophysics 55 (2): 282-286. https://doi.org/10.1002/2017RG000565

989 Chinn, D.S.; Isacks, B.I. 1983. Accurate source depths and focal mechanisms of shallow
990 earthquakes in western South America and in the New Hebrides Island arc. Tectonics 2:
991 529-563.

992 Costa, C.; Alvarado, A.; Audemard, F.; Audin, L.; Benavente, C.; Hilario Bezerra, F.;
993 Cembrano, J.; González, G.; López, M.; Minaya, E.; Santibañez, I.; Garcia J.; Acrila, M.;
994 Pagani, M.; Pérez, I.; Delgado, F.; Paolini, M.; Garro, H. 2020. Hazardous faults of South
995 America; compilation and overview. Journal of South American Earth Sciences 104.
996 https://doi.org/10.1016/j.jsames.2020.102837

997 De Pascale, G.; Froude, M.; Penna, I.; Hermanns, R.L.; Sepúlveda, S.A.; Moncada, D.;
998 Persico, M.; Easton, G.; Villalobos, A. A.; Gutierrez, F. 2021. Liquiñe-Ofqui's fast slipping
999 intra-volcanic arc crustal faulting above the subducted Chile Ridge. Scientific Reports 11.
1000 https://doi.org/10.1038/s41598-021-03919-z

1001 de Saint Blanquat, M.; Tikoff, B.; Teyssier, C.; Vigneresse, J.L. 1998. Transpressional
1002 kinematics and magmatic arcs. Geological Society, London, Special Publications 135:
1003 327-340. https://doi.org/10.1144/GSL.SP.1998.135.01.21

1004 Eisermann, J.O.; Göllner, P.L.; Riller, U. 2021. Orogen-scale transpression accounts for
1005 GPS velocities and kinematic partitioning in the Southern Andes. Communications Earth
1006 & Environment 2 167. https://doi.org/10.1038/s43247-021-00241-4

1007 Ekström, G.; Nettles, M; Dziewońsk, A.M. 2012. The global CMT project 2004–2010:
1008 Centroid-moment tensors for 13,017 earthquakes. Physics of the Earth and Planetary
1009 Interiors 200: 1-9. https://doi.org/10.1016/j.pepi.2012.04.002

1010 Farías, M.; Comte, D.; Charrier, R. 2006. Sismicidad superficial en Chile central:
1011 Implicancias para el estado cortical y crecimiento de los Andes Centrales australes. In
1012 Congreso Geológico Chileno, No. 11, Actas 1: 403–406. Antofagasta, Chile.

1013 Farías, M.; Charrier, R.; Carretier, S.; Martinod, J.; Fock, A.; Campbell, D.; Cáceres, J.;
1014 Comte, D. 2007. Late Miocene high and rapid surface uplift and its erosional response in
1015 the Andes of central Chile (33ºS-35ºS). Tectonics 27 (1): 1-22.
1016 https://doi.org/10.1029/2006TC002046

1017 Farías, M.; Comte, D.; Roecker, S.; Carrizo, D.; Pardo, M. 2011. Crustal extensional faulting
1018 triggered by the 2010 Chilean earthquake: The Pichilemu Seismic Sequence. Tectonics
1019 30 (6): 1-11. https://doi.org/10.1029/2011TC002888

1020 Fitch, T.J. 1972. Plate convergence, transcurrent fault, and internal deformation adjacent to
1021 Southeast Asia and the Western Pacific. Journal of Geophysical Research 77 (23): 4432-
1022 4460.

1023 Folguera, A.; Ramos, V.A.; Melnick, D. 2002. Partición de la deformación en la zona del arco
1024 volcánico de los Andes neuquinos (36-39ºS) en los últimos 30 millones de años. Revista
1025 Geológica de Chile 29 (2): 151-165. http://dx.doi.org/10.4067/S0716-
1026 02082002000200005

1027 Folguera, A.; Ramos, V.A.; Hermanns, R.L.; Naranjo, J. 2004. Neotectonics in the foothills of
1028 the southernmost central Andes (37º-38ºS): evidence of strike-slip displacement along the
1029 Antiñir-Copahue fault zone. Tectonics 23 (5): 1-23.
1030 https://doi.org/10.1029/2003TC001533

1031 Folguera, A.; Introcaso, A.; Gimenez, M.E.; Ruiz, F.; Martinez, M.P.; Tunstall, C.; Garcia
1032 Morabito, E.; Ramos, V.A. 2007. Crustal attenuation in the Southern Andean retroarc
1033 (38º-39º30'S) determined from tectonic and gravimetric studies: The Lonco-Luán
1034 asthenospheric anomaly. Tectonophysics 439(1); 129-147.
1035 https://doi.org/10.1016/j.tecto.2007.04.001

1036 Fondriest, M.; Mecklenburgh, J.; Passelegue, F.X.; Artioli, G.; Nestola, F.; Spagnuolo, E.;
1037 Rempe, M.; Di Toro, G,. 2020. Pseudotachylyte alteration and the rapid fade of
1038 earthquake scars from the geological record. Geophysical Research Letters 47 (22): 1-9.
1039 https://doi.org/10.1029/2020GL090020

1040 Forsythe, R.; Nelson, E. 1985. Geological manifestations of ridge collision: Evidence from
1041 the Golfo de Penas-Taitao Basin, Southern Chile. Tectonics 4 (5): 477-495.
1042 https://doi.org/10.1029/TC004i005p00477

1043 Galland, O.; Hallot, E.; Cobbold, P.R.; Ruffet, G.; d'Ars, J.d.B. 2007. Volcanism in a
1044 compressional Andean setting; a structural and geochronological study of Tromen
1045 volcano (Neuquén province, Argentina). Tectonics 26 (4): 1-24.
1046 https://doi.org/10.1029/2006TC002011

1047 García, A.R.; Beck, M.E.; Burmester, R.F.; Munizaga, F.E.; Hervé, F. 1988. Paleomagnetic
1048 reconnaissance of the Region de Los Lagos, Southern Chile, and its tectonic implications:
1049 Revista Geológica de Chile 15 (1): 13- 30.

1050 Gerbault, M.; Cembrano, J.; Mpodozis, C.; Farías, M.; Pardo, M. 2009. Continental margin
1051 deformation along the Andean subduction zone: Thermo-mechanical models. Physics of
1052 the Earth and Planetary Interiors 177: 180-205. https://doi.org/10.1016/j.pepi.2009.09.001

1053 Gerstenberger, M.C.; Marzocchi, W.; Allen, T.; Pagani, M.; Adams, J.; Danciu, L.; Field,
1054 E.H.; Fujiwara, H.; Luco, N.; Ma, K.-F.; Meletti, C.; Petersen, M.D. 2020. Probabilistic
1055 seismic hazard analysis at regional and national scales: State of the art and future
1056 challenges. Reviews of Geophysics 58 (2): e2019RG000653.
1057 https://doi.org/10.1029/2019RG000653

Gerstenberger, M. C.; Bora, S.; Bradley, B. A.; DiCaprio, C.; Kaiser, A.; Manea, E.F.; Nicol, A.; Rollins, C.; Stirling, M.W.; Thingbaijam, K.K.S.; Van Dissen, R.J.; Abbott, E.R.; Atkinson, G.M.; Chamberlain, C.; Christophersen, A.; Clark, K.; Coffey, G.L.; de la Torre, C.A.; Ellis, S.M.; Fraser, J.; Graham, K.; Griffin, J.; Hamling, I.J.; Hill, M.P.; Howell, A.; Hulsey, A.; Hutchinson, J.; Iturrieta, P.; Johnson, K.M.; Oakley Jurgens, V.; Kirkman, R.; Langridge, R.M.; Lee, R.L.; Litchfield, N.L.; Maurer, J.; Milner, K.R.; Rastin, S.; Rattenbury, M.S.; Rhoades, D.A.; Ristau, J.; Schorlemmer, D.; Seebeck, H.; Shaw, B.E.; Stafford, P.J.; Stolte, A.C.; Townend, J.; Villamor, P.; Wallace, L.M.; Weatherill, G.; Williams, C.A.; Wotherspoon, L.M. 2024. The 2022 Aotearoa New Zealand national seismic hazard model: Process, overview, and results. Bulletin of the Seismological Society of America, 114(1): 7-36. https://doi.org/10.1785/0120230182

Giambiagi, L.B.; Ramos, V.A. 2002. Structural evolution of the Andes in a transitional zone between flat and normal subduction (33º30'-33º45'S), Argentina and Chile. Journal of South American Earth Sciences 15 (1): 101-116. https://doi.org/10.1016/S0895-9811(02)00008-1

Giambiagi, L.; Mescua, J.; Bechis, F.; Tassara, A.; Hoke, G. 2012. Thrust belts of the southern Central Andes: Along-strike variations in shortening, topography, crustal geometry, and denudation. GSA Bulletin 124 (7-8): 1339-1351. https://doi.org/10.1130/B30609.1

Glodny, J.; Echtler, H.; Collao, S.; Ardiles, M.; Burón, P.; Figueroa, O. 2008. Differential Late Paleozoic active margin evolution in South-Central Chile (37ºS-40ºS) -The Lanalhue Fault Zone. Journal of South American Earth Sciences 26 (4): 397-411. https://doi.org/10.1016/j.jsames.2008.06.001

González, G.; Allmendinger, R.; Dunai, T.; Cembrano, J.; Martinod, J.; Rémy, D.; Carrizo, D.; Loveless, J.P.; Veloso, E.E.; Aron, F.; Cortés-Aranda, J. 2008. The active upper plate deformation of the Central Andes forearc, northern Chile: the geological view. In International Symposium on Andean Geodynamics (ISAG), No. 7, Extended Abstracts: 116–119. Nice, France.

Gratier, J.P.; Gamond, J.F. 1990. Transition between seismic and aseismic deformation in the upper crust. Geological Society, London, Special Publications 54: 461-473. https://doi.org/10.1144/GSL.SP.1990.054.01.42

Gratier, J.P.; Richard, J.; Renard, F.; Mittempergher, S.; Doan, M.L.; Di Toro, G.; Hadizadeh, J.; Boullier, A.M. 2011. Aseismic sliding of active faults by pressure solution creep: Evidence from the San Andreas Fault Observatory at depth. Geology 39 (12): 1131-1134. https://doi.org/10.1130/G32073.1

Hayes, G. P.; Moore, G. L.; Portner, D. E.; Hearne, M.; Flamme, H.; Furtney, M.; Smoczyk, G.M. 2018. Slab2, a comprehensive subduction zone geometry model. Science 362 (6410): 58-61. https://doi.org/10.1126/science.aat4723

Hernández-Moreno, C.; Speranza, F.; Di Chiara, A. 2014. Understanding kinematics of intra-arc transcurrent deformation: Paleomagnetic evidence from the Liquiñe-Ofqui fault zone (Chile, 38-41ºS). Tectonics 33 (10): 1964-1988. https://doi.org/10.1002/2014TC003622

1099 Hernandez-Moreno, C., F. Speranza, and A. Di Chiara 2016. Paleomagnetic rotation pattern
1100 of the southern Chile fore-arc sliver (38° S–42° S): A new tool to evaluate plate locking
1101 along subduction zones, J. Geophys. Res. Solid Earth, 121, 469–490,
1102 doi:10.1002/2015JB012382.

1103 Hervé, M., 1976. Estudio geológico de la falla Liquiñe-Reloncaví en el área de Liquiñe-
1104 Reloncaví, antecedentes de un movimiento transcurrente (Provincia de Valdivia). I Congr.
1105 Geol. Chil. Actas, I: B39-B56.

1106 Hervé, F., Araya, E., Fuenzalida, J.L. and Solano, A., 1979. Edades radiométricas y
1107 tectónica neógena en el sector costero de Chiloé Continental, X Región. II Congr. Geol.
1108 Chil. Actas, 1: FI-F8.

1109 Hervé, F. 1994. The Southern Andes between 39° and 44° S Latitude: The Geological
1110 Signature of a Transpressive Tectonic Regime Related to a Magmatic Arc. In: Reutter,
1111 K.J., Scheuber, E. and Wigger, P.J., Eds., Tectonics of the Southern Central Andes,
1112 Springer Verlag, Berlin, 243-248. https://doi.org/10.1007/978-3-642-77353-2_1

1113 Hervé, F.; Pankhurst, R.J.; Drake, R.; Beck, M.E. 1995. Pillow metabasalts in a mid-Tertiary
1114 extensional basin adjacent to the Liquiñe-Ofqui fault zone: the Isla Magdalena area,
1115 Aysén, Chile. Journal of South American Earth Sciences 8 (1): 33-46.
1116 https://doi.org/10.1016/0895-9811(94)00039-5

1117 Iturrieta, P.C.; Hurtado, D.E.; Cembrano, J.; Stanton-Yonge, A. 2017. States of stress and
1118 slip partitioning in a continental-scale strike-slip duplex: Tectonic and magmatic
1119 implications by means of finite element modeling. Earth and Planetary Science Letters
1120 473 (1): 71-82. https://doi.org/10.1016/j.epsl.2017.05.041

1121 Jarrard, R.D. 1986. Relations among subduction parameters. Reviews of Geophysics 24 (2):
1122 217-284. https://doi.org/10.1029/RG024i002p00217

1123 Johnson, S.Y.; Blakely, R.J.; Stephenson, W.J.; Dadisman, S.V.; Fisher, M.A. 2004. Active
1124 shortening of the Cascadia forearc and implications for seismic hazards of the Puget
1125 Lowland. Tectonics 23 (1): 1-27. https://doi.org/10.1029/2003TC001507

1126 Jordan, T.E.; Isacks, B.L.; Allmendinger, R.W.; Brewer, J.A.; Ramos, V.A.; Ando, C.J. 1983.
1127 Andean tectonics related to geometry of subducted Nazca plate. GSA Bulletin 94: 341-
1128 361.: 297-306. https://doi.org/10.1130/0016-
1129 7606(1983)94%3C341:ATRTGO%3E2.0.CO;2

1130 Kirkpatrick, J.D.; Rowe, C.D. 2013. Disappearing ink: How pseudotachylytes are lost from
1131 the rock record. Journal of Structural Geology 52: 183-198.
1132 https://doi.org/10.1016/j.jsg.2013.03.003

1133 Lange, D.; Cembrano, J.; Rietbrock, A.; Haberland, C.; Dahm, T.; Bataille, K. 2008. First
1134 seismic record for intra-arc strike-slip tectonics along the Liquiñe-Ofqui fault zone at the
1135 obliquely convergent plate margin of the southern Andes. Tectonophysics 445 (1-4): 14-
1136 24. https://doi.org/10.1016/j.tecto.2008.04.014

1137 Lara, L.E.; Naranjo, J.A.; Moreno, H. 2004. Rhyodacitic fissure eruption in the Southern
1138 Andes (Cordón Caulle; 40.5° S) after the 1960 (Mw 9.5) Chilean earthquake: A structural
1139 interpretation. Journal of Volcanology and Geothermal Research 138 (1–2): 127–138.
1140 https://doi.org/10.1016/j.jvolgeores.2004.06.009

1141 Lara, L.; Lavenu, A.; Cembrano, J.; Rodríguez, C. 2006. Structural controls of volcanism in
1142 transversal chains: Resheared faults and neotectonics in the Cordón Caulle-Puyehue
1143 area (40.5ºS), Southern Andes. Journal of Volcanology and Geothermal Research 158 (1-
1144 2): 70-86. https://doi.org/10.1016/j.jvolgeores.2006.04.017

1145 Lavenu, A.; Cembrano, J. 1999. Compressional- and transpressional-stress pattern for
1146 Pliocene and Quaternary brittle deformation in fore arc and intra-arc zones (Andes of
1147 Central and Southern Chile). Journal of Structural Geology 21: 1669-1691.
1148 https://doi.org/10.1016/S0191-8141(99)00111-X

1149 Lavenu, A.; Thiele, R.; Machette, M.; Dart, R.; Bradley, L.-A.; Haller, K.M. 2000. Maps and
1150 database of Quaternary faults in Bolivia and Chile. U.S. Geological Survey, Open-File
1151 Report 00-283: 46 p.

1152 Lavenu, A.; Cembrano, J. 2008. Quaternary compressional deformation in the Main
1153 Cordillera of Central Chile (Cajón del Maipo, east of Santiago). Revista Geológica de
1154 Chile 35 (2): 233-252. http://dx.doi.org/10.5027/andgeoV35n2-a03

1155 Legrand, D.; Barrientos, S.; Bataille, K.; Cembrano, J.; Pavez, A. 2011. The fluid-driven
1156 tectonic swarm of Aysen Fjord, Chile (2007) associated with two earthquakes (Mw=6.1
1157 and Mw=6.2) within the Liquiñe-Ofqui Fault Zone. Continental Shelf Research 31 (3-4):
1158 154-161. https://doi.org/10.1016/j.csr.2010.05.008

1159 Lockner, D.A. 1995. Rock failure. Rock physics and phase relations: A handbook of physical
1160 constants (3):127-147.

1161 Maldonado, V.; Contreras, M.; Melnick, D. 2021. A comprehensive database of active and
1162 potentially-active continental faults in Chile at 1:25,000 scale. Scientific Data 8 (20).
1163 https://doi.org/10.1038/s41597-021-00802-4

1164 Marrett, R.; Allmendinger, R.W. 1990. Kinematic analysis of fault-slip data. Journal of
1165 Structural Geology 12 (8): 973-986. https://doi.org/10.1016/0191-8141(90)90093-E

1166 McCaffrey, R. 1992. Oblique plate convergence, slip vectors, and forearc deformation.
1167 Journal of Geophysical Research Atmospheres 97 (B6): 8905-8915.
1168 https://doi.org/10.1029/92JB00483

1169 McCaffrey, R. 1996. Slip partitioning at convergent plate boundaries of SE Asia. Geological
1170 Society, London, Special Publications 106: 3-18.
1171 https://doi.org/10.1144/GSL.SP.1996.106.01.02

1172 Melnick, D.; Charlet, F.; Echtler, H.P., De Batist, M. 2006. Incipient axial collapse of the Main
1173 Cordillera and strain partitioning gradient between the central and Patagonian Andes,
1174 Lago Laja, Chile. Tectonics 25 (5): 1-22. https://doi.org/10.1029/2005TC001918

Melnick, D.; Bookhagen, B.; Strecker, M.R.; Echtler, H.P. 2009. Segmentation of megathrust rupture zones from fore-arc deformation patterns over hundreds to millions of years, Arauco peninsula, Chile. Journal of Geophysical Research 114 (B1): B01407. https://doi.org/10.1029/2008JB005788

Mescua, J.F.; Barrionuevo, M.; Giambiagi, L.; Suriano, J.; Spagnotto, S.; Stahlschmidt, E.; de la Cal, H.; Soto, J.L.; Mazzitelli, M.A. 2019. Stress field and active faults in the orogenic front of the Andes in the Malargüe fold-and-thrust belt (35º-36ºS). Tectonophysics 766: 179-193. https://doi.org/10.1016/j.tecto.2019.06.003

Montenegro, V.M.; Spagnotto, S.; Legrand, D.; Caselli, A.T. 2021. Seismic evidence of the active regional tectonic faults and the Copahue volcano, at Caviahue Caldera, Argentina. Bulletin of Volcanology 83 (20). https://doi.org/10.1007/s00445-021-01442-7

Mora, C.; Comte, D.; Russo, R.; Gallego, A.; Mocanu, V. 2010. Aysén seismic swarm (January 2007) in southern Chile: analysis using Joint Hypocenter Determination. Journal of Seismology 14: 683-691. https://doi.org/10.1007/s10950-010-9190-y

Moreno, M.S.; Bolte, J.; Klotz, J.; Melnick, D. 2009. Impact of megathrust geometry on inversion of coseismic slip from geodetic data: Application to the 1960 Chile earthquake. Geophysical Research Letters 36 (16). https://doi.org/10.1029/2009GL039276

Moreno, M.; Melnick, D.; Rosenau, M.; Baez, J.; Klotz, J.; Oncken, O.; Tassara, A.; Chen, J.; Bataille, K.; Bevis, M.; Socquet, A.; Bolte, J.; Vigny, C.; Brooks, B.; Ryder, I.; Grund, V.; Smalley, B.; Carrizo, D.; Bartsch, M.; Hase. H. 2012. Toward understanding tectonic control on the Mw 8.8 2010 Maule Chile earthquake. Earth and Planetary Science Letters 321-322: 152-165. https://doi.org/10.1016/j.epsl.2012.01.006

Moreno, M.; Bedford, J.R.; Schurr, B.; Baez, J.C.; Urrutia, I.; Lange, D.; Oncken, O.; Melnick, D. 2016. From locking to coupling: Investigating the links between kinematics and stress accumulation along the Chilean subduction Zone. AGU Fall Meeting Abstracts, 2016.

Mura, V.; Arancibia, G.; Browning, J.; Healy, D.; López-Contreras, C.; Morata, D.; Maza, S.; Cardona, C. 2025. Structural control on the Southern Andean Nevados de Chillán geothermal system. Journal of Structural Geology 196. https://doi.org/10.1016/j.jsg.2025.105380

Niemeijer, A.; Di Toro, G.; Nielsen, S.; Di Felice, F. 2011. Frictional melting of gabbro under extreme experimental conditions of normal stress, acceleration, and sliding velocity. Journal of Geophysical Research: Solid Earth 116 (7): 1-18. https://doi.org/10.1029/2010JB008181

Noda, H.; Lapusta, N. 2013. Stable creeping fault segments can become destructive as a result of dynamic weakening. Nature 493: 518-521. https://doi.org/10.1038/nature11703

Olivar, J.; Nacif, S.; García, H.; Fennell, L.; Heit, B.; Folguera, A. 2022. Controls on crustal seismicity segmentation on a local scale in the Southern Central Andes. Journal of South American Earth Sciences 116: 103778. https://doi.org/10.1016/j.jsames.2022.103778

1213 Pardo-Casas, F.; Molnar, P. 1987. Relative motion of the Nazca (Farallon) and South
1214 American plates since late Cretaceous time. Tectonics 6 (3): 233-248.
1215 https://doi.org/10.1029/TC006i003p00233

1216 Pearce, R.K.; Sánchez de la Muela, A.; Moorkamp, M.; Hammond, J.O.S.; Mitchell, T.M.;
1217 Cembrano, J.; Araya Vargas, J.; Meredith, P.G.; Iturrieta, P.; Pérez-Estay, N.; Marshall,
1218 N.R.; Smith, J.; Yañez, G.; Griffith, W.A.; Marquardt, C.; Stanton-Yonge, A.; Núñez, R.
1219 2020. Reactivation of fault systems by compartmentalized hydrothermal fluids in the
1220 Southern Andes revealed by magnetotelluric and seismic data. Tectonics 39:
1221 e2019TC005997. https://doi.org/10.1029/2019TC005997

1222 Pérez-Estay, N.; Yáñez, G.; Crempien, J.; Roquer, T.; Cembrano, J.; Valdenegro, P.;
1223 Aravena, D.; Arancibia, G.; Morata, D. 2020. Seismicity in a transpressional volcanic arc:
1224 The Liquiñe-Ofqui Fault System in the Puyuhuapi Area, Southern Andes, Chile (44ºS).
1225 Tectonics 39: e2020TC006391. https://doi.org/10.1029/2020TC006391

1226 Pérez-Estay, M.; Ruz-Ginouves, J.; Pérez-Flores, P.; Sielfeld, G.; Roquer, T.; Cembrano, J.
1227 2023. Decoding the state of stress and fluid pathways along the Andean Southern
1228 Volcanic Zone. Communications Earth & Environment 4: 390.
1229 https://doi.org/10.1038/s43247-023-01040-9

1230 Pérez-Flores, P.; Cembrano, J.; Sánchez-Alfaro, P.; Veloso, E.; Arancibia, G.; Roquer, T.
1231 2016. Tectonics, magmatism and paleo-fluid distribution in a strike-slip setting: Insights
1232 from the northern termination of the Liquiñe-Ofqui fault System, Chile. Tectonophysics
1233 680: 192-210. https://doi.org/10.1016/j.tecto.2016.05.016

1234 Petit, J.P. 1987. Criteria for the sense of movement on fault surfaces in brittle rocks. Journal
1235 of Structural Geology 9 (5-6): 597-608. https://doi.org/10.1016/0191-8141(87)90145-3

1236 Piquer, J.; Castelli, J.C.; Charrier, R.; Yáñez, G. 2010. The Cenozoic of the upper Teno
1237 River, Cordillera Principal, Central Chile: stratigraphy, plutonism and their relation with
1238 deep structures. Andean Geology 37 (1): 32-53. http://dx.doi.org/10.5027/andgeoV37n1-
1239 a2

1240 Piquer, J.; Skarmeta, J.; Cooke, D.R. 2015. Structural evolution of the Rio Blanco-Los
1241 Bronces District, Andes of Central Chile: controls on stratigraphy, magmatism, and
1242 mineralization. Economic Geology 110 (8): 1995-2023.
1243 https://doi.org/10.2113/econgeo.110.8.1995

1244 Piquer, J.; Rivera, O.; Yáñez, G.; Oyarzún, N. 2021. The Piuquencillo fault system: a long-
1245 lived, Andean-transverse fault system and its relationship with magmatic and
1246 hydrothermal activity. Solid Earth 12 (1): 253-273. https://doi.org/10.5194/se-12-253-2021

1247 Potin, B.; Ruiz, S.; Aden-Antoniow, F.; Madariaga, R.; Barrientos, S. 2025. A revised Chilean
1248 seismic catalog from 1982 to mid-2020. Seismological Research Letters, *96* (1): 484-498.
1249 https://doi.org/10.1785/0220240047

Quiero, F.; Tassara, A.; Iaffaldano, G.; Rabbia, O. 2022. Growth of Neogene Andes linked to changes in plate convergence using high-resolution kinematic models. Nature Communications 13: 1339. https://doi.org/10.1038/s41467-022-29055-4

Ramos, V. A.; Jordan, T. E.; Allmendinger, R. W.; Mpodozis, C.; Kay, S. M. ; Cortés, J.M. ; Palma, M. 1986. Paleozoic terranes of the central Argentine-Chilean Andes. Tectonics, 5(6): 855-880. https://doi.org/10.1029/TC005i006p00855

Rivera, O.; Cembrano, J. 2000. Modelo de formación de cuencas volcano-tectónicas en zonas de transferencia oblicuas a la cadena andina: El caso de las cuencas oligo-miocénicas de Chile central y su relación con estructuras NWW-NW (33º00'-34º30'S). In Congreso Geológico Chileno, No. 9, Actas 1:631-636. Puerto Varas, Chile.

Rojas, C.; Beck Jr., M.E.; Burmester, R.F.; Cembrano, J.; Hervé, F. 1994. Paleomagnetism of the Mid-Tertiary Ayacara Formation, southern Chile: counterclockwise rotation in a dextral shear zone. Journal of South American Earth Sciences 7 (1): 45-56. https://doi.org/10.1016/0895-9811(94)90033-7

Rosenau, M.; Melnick, D.; Echtler, H. 2006. Kinematic constraints on intra-arc shear and strain partitioning in the southern Andes between 38ºS and 42ºS latitude. Tectonics 25 (4): 1-16. https://doi.org/10.1029/2005TC001943

Rousset, B. 2019. Months-long subduction slow slip events avoid the stress shadows of seismic asperities. Journal of Geophysical Research: Solid Earth 124 (7): 7337-7230. https://doi.org/10.1029/2019JB018037

Rowe, C.D.; Griffith, W.A. 2015. Do faults preserve a record of seismic slip? A second opinion. Journal of Structural Geology 78: 1-26. https://doi.org/10.1016/j.jsg.2015.06.006

Rowland, J.V.; Simmons, S.F. 2012. Hydrologic, magmatic, and tectonic controls on hydrothermal flow, Taupo Volcanic Zone, New Zealand: Implications for the formation of epithermal vein deposits. Economic Geology 107 (3): 427-457. https://doi.org/10.2113/econgeo.107.3.427

Rutter, E.H. 1983. Pressure solution in nature, theory and experiment. Journal of the Geological Society 140 (5): 725-740. https://doi.org/10.1144/gsjgs.140.5.0725

Ruz-Ginouves, J.; Browning, J.; Cembrano, J.; Iturrieta, P.; Gerbault, M.; Sielfeld, G. 2020. Field observations and numerical models of a Pleistocene-Holocene feeder dyke swarm associated with a fissure complex to the east of the Tatara-San Pedro-Pellado complex, Southern Volcanic Zone, Chile. Journal of Volcanology and Geothermal Research 404. https://doi.org/10.1016/j.jvolgeores.2020.107033

Sánchez, P.; Pérez-Flores, P.; Arancibia, G.; Cembrano, J.; Reich, M. 2013. Crustal deformation effects on the chemical evolution of geothermal systems-. The intra-arc Liquiñe-Ofqui fault system, Southern Andes. International Geology Review 55 (11): 1384-1400. https://doi.org/10.1080/00206814.2013.775731

Santibañez, I.; Cembrano, J.; García-Pérez, T.; Costa, C.; Yáñez, G.; Marquardt, C.; Arancibia G.; González, G. 2019. Crustal faults in the Chilean Andes: geological

constraints and seismic potential. Andean Geology 46 (1): 32-68. http://dx.doi.org/10.5027/andgeoV46n1-3067

Savran, W. H.; Bayona, J. A.; Iturrieta, P.; Asim, K. M.; Bao, H.; Bayliss, K.; Herrmann, M.; Schorlemmer, D.; Marchling, P.J.; Werner, M.J. 2022. pyCSEP: A Python toolkit for earthquake forecast developers. Seismological Society of America, 93(5): 2858-2870. https://doi.org/10.1785/0220220033

Seebeck, H.; Van Dissen, R.; Litchfield, N.; Barnes, P.M.; Nicol, A. Langridge, R.; Barrell, D.J.A.; Villamor, P.; Ellis, S.; Rattenbury, M.; Bannister, S.; Gerstenberger, M.; Ghisetti, F.; Sutherland, R.; Hirschberg, H.; Fraser, J.; Nodder, S.D.; Stirling, M.; Humphrey, J.; Bland, K.J.; Howell, A.; Mountjoy, J.; Moon, V.; Stahl, T.; Spinardi, F.; Townsend, D.; Clark, K.; Hamling, I.; Cox, S.; de Lange, W.; Wopereis, P.; Johnston, M.; Morgenstern, R.; Coffey, G.; Eccles, J.D.; Little, T.; Fry, B.; Griffin, J.; Townend, J.; Mortimer, N.; Alcaraz, S.; Massiot, C.; Rowland, J.V.; Muirhead, J.; Upton, P.; Lee, J. 2023. The New Zealand Community Fault Model–version 1.0: An improved geological foundation for seismic hazard modelling. New Zealand Journal of Geology and Geophysics 67 (2): 209-229. https://doi.org/10.1080/00288306.2023.2181362

Sernageomin. 2003. Mapa Geológico de Chile: versión digital. Servicio Nacional de Geología y Minería, Publicación Geológica Digital No. 4 (CD-ROM, versión 1.0, 2003). Santiago, Chile.

Sielfeld, G.; Cembrano, J.; Lara, L. 2017. Transtension driving volcano-edifice anatomy: Insights from Andean transverse-to-the-orogen tectonic domains. Quaternary International 438: 33-49. https://doi.org/10.1016/j.quaint.2016.01.002

Sielfeld, G.; Lange, D.; Cembrano, J. 2019a. Intra-arc crustal seismicity: Seismotectonic implications for the Southern Andes Volcanic Zone, Chile. Tectonics 38: 552-578. https://doi.org/10.1029/2018TC004985

Sielfeld, G.; Ruz, J.; Brogi, A.; Cembrano, J.; Stanton-Yonge, A.; Pérez-Flores, P.; Iturrieta, P. 2019b. Oblique-slip tectonics in an active volcanic chain: A case study from the Southern Andes. Tectonophysics 770. https://doi.org/10.1016/j.tecto.2019.228221

Somoza, R. 1998. Updated Nazca (Farallon) – South America relative motions during the last 40 My: implications for mountain building in the central Andean region. Journal of South American Sciences 11 (3): 211-215. https://doi.org/10.1016/S0895-9811(98)00012-1

Stanton-Yonge, A.; Griffith, W.A.; Cembrano, J.; St. Julien, R.; Iturrieta, P. 2016. Tectonic role of margin-parallel and margin-transverse faults during oblique subduction in the Southern Volcanic Zone of the Andes: Insights from Boundary Element Modeling. Tectonics 35: 1990-2013. https://doi.org/10.1002/2016TC004226

Stanton-Yonge, A.; Sánchez de la Muela, A.; Pearce, R.K.; Hammond, J.O.S.; Mitchell, T.M.; Hicks, S.P.; Griffith, W.A. ; Moorkamp, M. ; Meredith, P.; Cembrano, J. 2025. Fluid pressure fluctuations and the seismic signature of a fault-controlled fluid migration pulse. Earth and Planetary Science Letters 662. https://doi.org/10.1016/j.epsl.2025.119388

Stern, C.R.; Skewes, M.A.; Arévalo, A. 2011. Magmatic evolution of the giant El Teniente Cu-Mo Deposit, Central Chile. Journal of Petrology 52 (7-8): 1591-1617. https://doi.org/10.1093/petrology/egq029

Tapia, F.; Farías, M.; Naipauer, M.; Puratich, J. 2015. Late Cenozoic contractional evolution of the current arc-volcanic region along the southern Central Andes (35°20'S). Journal of Geodynamics 88: 36–51. https://doi.org/10.1016/j.jog.2015.01.001

Tassara, A.; Yáñez, G. 2003. Relación entre el espesor elástico de la litósfera y la segmentación tectónica del margen andino (15-47ºS). Andean Geology 30 (2): 159-186. http://dx.doi.org/10.4067/S0716-02082003000200002

Teyssier, C.; Tikoff, B.; Markley, M. 1995. Oblique plate motion and continental tectonics. Geology 23 (5): 447-450. https://doi.org/10.1130/0091-7613(1995)023%3C0447:OPMACT%3E2.3.CO;2

Thompson, S.N. 2002. Late Cenozoic geomorphic and tectonic evolution of the Patagonian Andes between latitudes 42ºS and 46ºS: An appraisal based on fission-track results from the transpressional intra-arc Liquiñe-Ofqui fault zone. GSA Bulletin 114 (9): 1159-1173. https://doi.org/10.1130/0016-7606(2002)114%3C1159

U.S. Geological Survey (USGS). 2017. Advanced National Seismic System (ANSS) Comprehensive Earthquake Catalog. https://earthquake.usgs.gov/data/comcat/

Vega-Ruiz, A.; Cortés-Aranda, J.; Aguilera-Cortés, R.; Astudillo-Sotomayor, L.; Riedel, M.; Espinoza, M.; Tassara, A.; Nelson, A.; Melnick, D.; Lupi, M.; Arriagada, S.; Spúlveda, T.; Álvarez-Amado, F.; Navarro, L. 2025. Pliocene to Holocene deformation and earthquake potential of the Mesamávida Fault, West Andean Thrust System of Central-Southern Chile (36° S). Tectonics 44 (7): e2025TC008848. https://doi.org/10.31223/X5T153

Vargas, G.; Klinger, Y.; Rockwell, T.K.; Forman, S.L.; Rebolledo, S.; Baize, S.; Lacassin, R.; Armijo, R. 2014. Probing large intraplate earthquakes at the west flank of the Andes. Geology 42 (12): 1083-1086. https://doi.org/10.1130/G35741.1

Vigide, N.; Olivar, J.; Mescua, J.; Basualto, D.; Farías, C.; Tassara, A.; García, S. 2025. A transpressive stress regime for the Laguna del Maule Volcanic Complex. Journal of South American Earth Sciences 161: 105563. https://doi.org/10.1016/j.jsames.2025.105563

Vigny, C.; Socquet, A.; Peyrat, S.; Ruegg, J.C.; Métois, M.; Madariaga, R.; Morvan, S.; Lancieri, M.; Lacassin, R.; Campos, J.; Carrizo, D.; Bejar-Pizarro, M.; Barrientos, S.; Armijo, R.; Aranda, C.; Valderas-Bermejo, M.-C.; Ortega, I.; Bondoux, F.; Baize, S.; Lyon-Caen, H.; Pavez, A.; Vilotte, J.P.; Bevis, M.; Brooks, B.; Smalley, R.; Parra, H.; Baez, J.-C.; Blanco, M.; Cimbaro, S.; Kendrick, E. 2011.The 2010 Mw 8.8 Maule Megathrust earthquake of Central Chile, monitored by GPS. Science 332 (6036): 1417-1421. https://doi.org/10.1126/science.1204132

Wall R.; Gana, P.; Gutiérrez, A. 1996. Mapa geológico del área de San Antonio-Melipilla, regiones de Valparaíso, Metropolitana y del Libertador General Bernardo O'Higgins.

Servicio Nacional de Geología y Minería, Mapas Geológicos N°2, escala 1:100.000, 1 mapa, 1 anexo.

Wang, K.; Hu, Y.; Bevis, M.; Kendrick, E.; Smalley Jr., R.; Barriga Vargas, R.; Lauría, E. 2007. Crustal motion in the zone of the 1960 Chile earthquake: Detangling earthquake-cycle deformation and forearc-sliver translation. Geochemistry, Geophysics, Geosystems 8 (10): 1-14. https://doi.org/10.1029/2007GC001721

Weatherill, G. A.; Pagani, M.; Garcia, J. 2016. Exploring earthquake databases for the creation of magnitude-homogeneous catalogues: tools for application on a regional and global scale. Geophysical Journal International 206.3: 1652-1676. https://doi.org/10.1093/gji/ggw232

Weller, O.; Lange, D.; Tilmann, F.; Natawidjaja, D.; Rietbrock, A.; Collings, R.; Gregory, L. 2012. The structure of the Sumatran Fault revealed by local seismicity. Geophysical Research Letters 39 (1): 1-7. https://doi.org/10.1029/2011GL050440

Yáñez, G.A.; Gana, P.; Fernández, R. 1998. Origen y significado geológico de la Anomalía Melipilla, Chile central. Revista Geológica de Chile 25 (2): 175-198. http://dx.doi.org/10.4067/S0716-02081998000200005

Yáñez, G.; Pérez-Estay, N.; Araya-Vargas, J.; Sanhueza, J.; Figueroa, R.; Maringue, J.; Rojas, T. 2020. Shallow anatomy of the San Ramón Fault (Chile) constrained by geophysical methods: Implications for its role in the Andean deformation. Tectonics 39 (8): 1-21. https://doi.org/10.1029/2020TC006294

Yáñez, G.; Piquer, J.; Rivera, O. 2024. On the role of trans-lithospheric faults in the long-term seismotectonic segmentation of active margins: a case study in the Andes. European Geosciences Union 15 (11): 1319-1342. https://doi.org/10.5194/se-15-1319-2024

Youngs, R.; Coppersmith, K. 1985. Implications of fault slip rates and earthquake recurrence models to probabilistic seismic hazard estimates. Bulletin of the Seismological Society of America 75 (4): 939-964. https://doi.org/10.1016/0148-9062(86)90651-0

Figure Captions

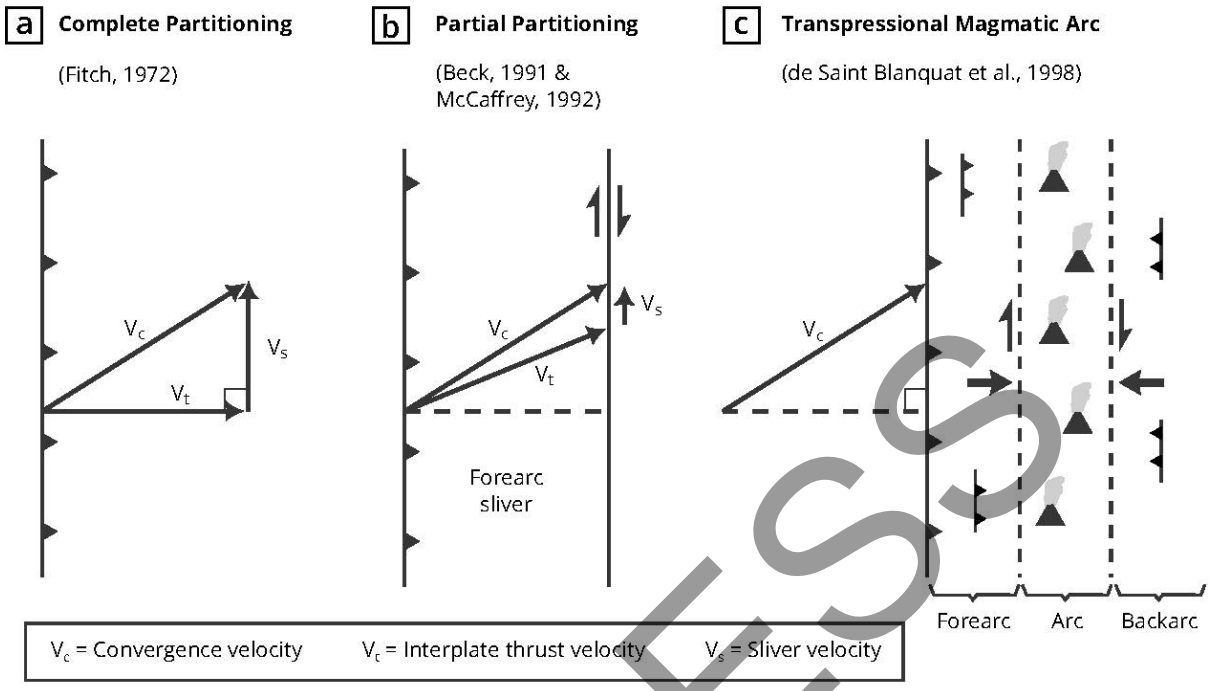

- **Fig. 1.** Schematic diagram illustrating the evolution of the slip partitioning concept over the past five decades. **A.** Complete partitioning of the convergence slip vector (Fitch, 1972). **B.** Partial partitioning (e.g., Beck, 1991; McCaffrey, 1992). **C.** Slip partitioning considering a transpressional magmatic arc domain (de Saint Blanquat et al., 1998).

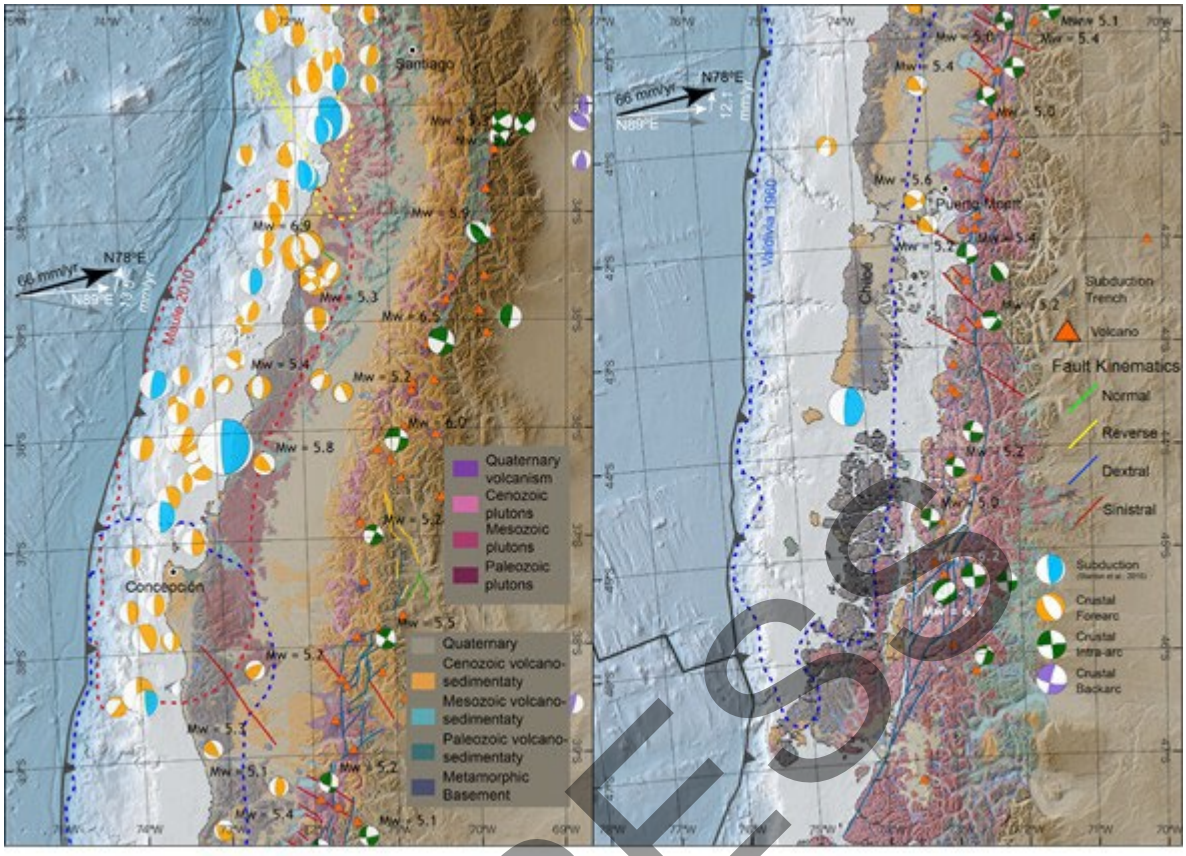

1402 ●

1403 ● **Fig. 2.** Tectonic, geological, and seismological setting of the Chilean Andes
1404 between 33° and 47° S, mainly based on Sernageomin (2003), Cembrano and
1405 Lara (2009), Tapia et al. (2015), Stanton-Yonge et al. (2016), Sielfeld et al.
1406 (2019a), and Olivar et al. (2022). Main Quaternary crustal faults (data from
1407 Santibáñez et al., 2019 and Costa et al., 2020), and Holocene volcanoes are
1408 included for reference. Crustal seismicity in the overriding plate is shown for
1409 earthquakes with Mw>5.0 based on data from global networks. Selection
1410 subduction interface events (Stanton-Yonge et al., 2016) are displayed alongside
1411 crustal seismicity. The segmented blue line indicates the rupture zone of the Mw
1412 9.5 1960 Valdivia earthquake (Moreno et al., 2009), the red segmented line
1413 marks the Mw 8.8 2010 Maule earthquake (Moreno et al., 2012), and the yellow
1414 segmented line shows the Mw 8.0 1985 Valparaíso earthquake (Bravo et al.,

2019). The partitioning of the convergence vector (N78°E, black arrow) into its margin-parallel and margin-orthogonal (grey arrows) components is depicted for the regions between 34° and 38° S (where the margin trends N20°E), and between 38° and 47° S (where the margin trends N10°E). The average slip vector of subduction earthquakes (N89°E; Stanton-Yonge et al., 2016) is also shown (white arrow in between the convergence vector and the orthogonal to the trench), illustrating the partial partitioning of convergence along the margin. The residual margin-parallel component to be accommodated within the overriding plate is indicated for both regions (white arrows parallel to the plate margin; 13.5 mm/year for 34°–38° S and 12.1 mm/year for 38°–47° S). The full classified catalog and the P- and T-axes for each earthquake class are shown respectively in figures S1 and S2 in the Supplementary Material. See the Data and Resources chapter for more information on data source compilation and processing.

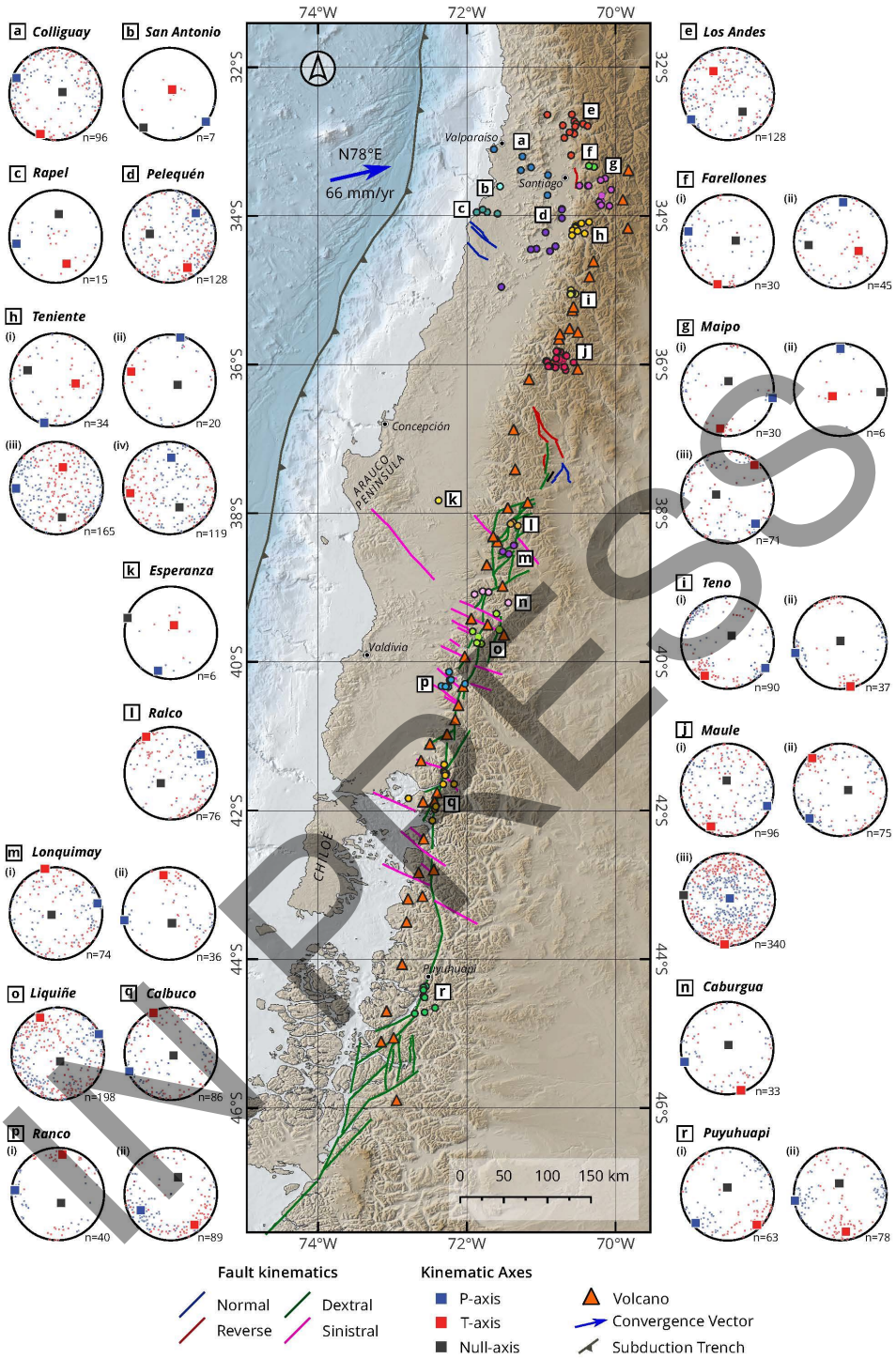
a Colliguay
b San Antonio
c Rapel
d Pelequén
h Teniente
k Esperanza
l Ralco
m Lonquimay
o Liquiñe
q Calbuco
p Ranco
e Los Andes
f Farellones
g Maipo
i Teno
j Maule
n Caburgua
r Puyuhuapi
74°W
72°W
70°W
32°S
34°S
36°S
38°S
40°S
42°S
44°S
46°S
N78°E
66 mm/yr
Valparaíso
Santiago
Concepción
ARAUCO PENINSULA
Valdivia
CHILOÉ
Puyuhuapi
0 50 100 150 km
Fault kinematics
Normal
Reverse
Dextral
Sinistral
Kinematic Axes
P-axis
T-axis
Null-axis
Volcano
Convergence Vector
Subduction Trench

- **Fig. 3.** Compilation and analysis of both published (e.g., Arancibia et al., 1999; Lavenu and Cembrano,1999; Pérez-Flores et al., 2016; Roquer et al., 2022) and new (this study) fault slip data. Structural sites, or combinations of them, are grouped in clusters in case of consistent P–T results (labelled A to R). On the map, each structural site is shown as a circle, colored by cluster group. Clusters with more than one distinct solution are displayed with multiple lower-hemisphere equal-area stereonets, labeled i to iv, depending on the number of additional solutions. All clusters show both the distribution of P and T instantaneous strain axis orientations for all individual faults (blue and red dots), as well as the kinematic axes for the fault population, calculated using the methods established after Marret and Allmendinger (1990) and Allmendinger et al. (2012). The maximum shortening axis (P), minimum shortening axis (T), and the null axis are represented as blue, red, and black squares, respectively. Red triangles represent active volcanoes.

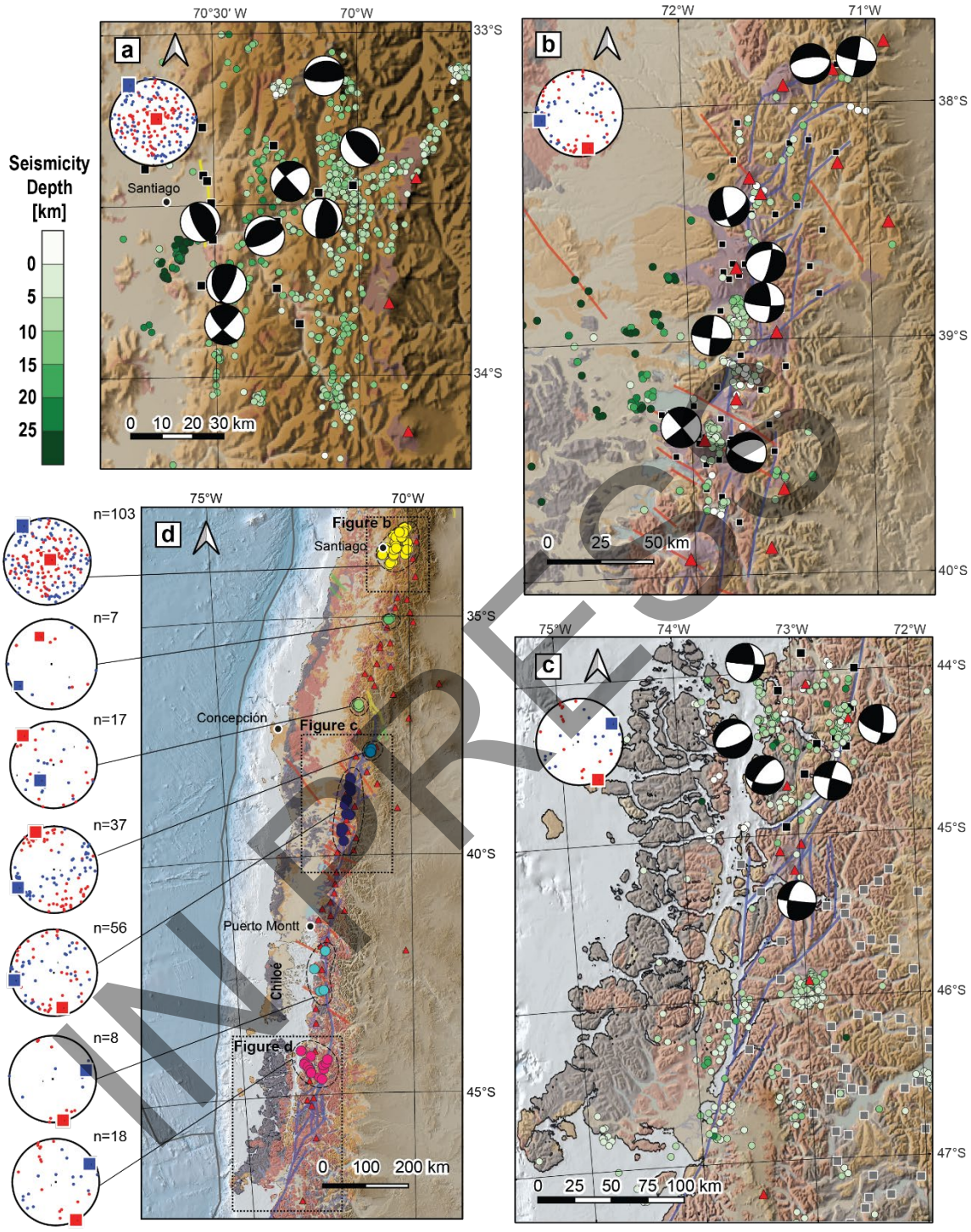

1443 ●

1444 ● **Fig. 4.** Compilation and analysis of published crustal seismicity and a subset of

1445 focal mechanisms from local seismic networks, including events with Mw<5.0.

1446 Black and gray squares mark seismic stations from temporary local network

deployments in previous studies, from which the data were compiled. Panels (**A**), (**B**), and (**C**) show insets with previously published seismicity for the Maipo, Araucanía, and Aysén regions, respectively. The Maipo region includes seismicity and focal mechanisms from Ammirati et al. (2019). The Araucanía region exhibits seismicity reported by Sielfeld et al. (2019a), along with focal mechanisms from the same authors and from Montenegro et al. (2021). The Aysén region shows seismicity reported by Agurto et al. (2014) and Pérez-Estay et al. (2020), accompanied by focal mechanisms from Mora et al. (2010) and Pérez-Estay et al. (2020), the latter referring to the initial state of the 2007 Aysén crisis. Panel (**D**) shows a regional map with the locations of individual seismic events (colored circles) for which focal mechanism solutions were obtained from different local seismic networks. Each local network is represented by a distinct color. Background geology and structures are as shown in figure 2. The stereonet plots summarize the P- and T-axis orientations of all mechanisms recovered by each local network, with blue and red squares indicating the average P- and T-axis directions for each network, respectively. For more information, the reader is referred to the literature cited in this study and to the Data and Resources chapter.

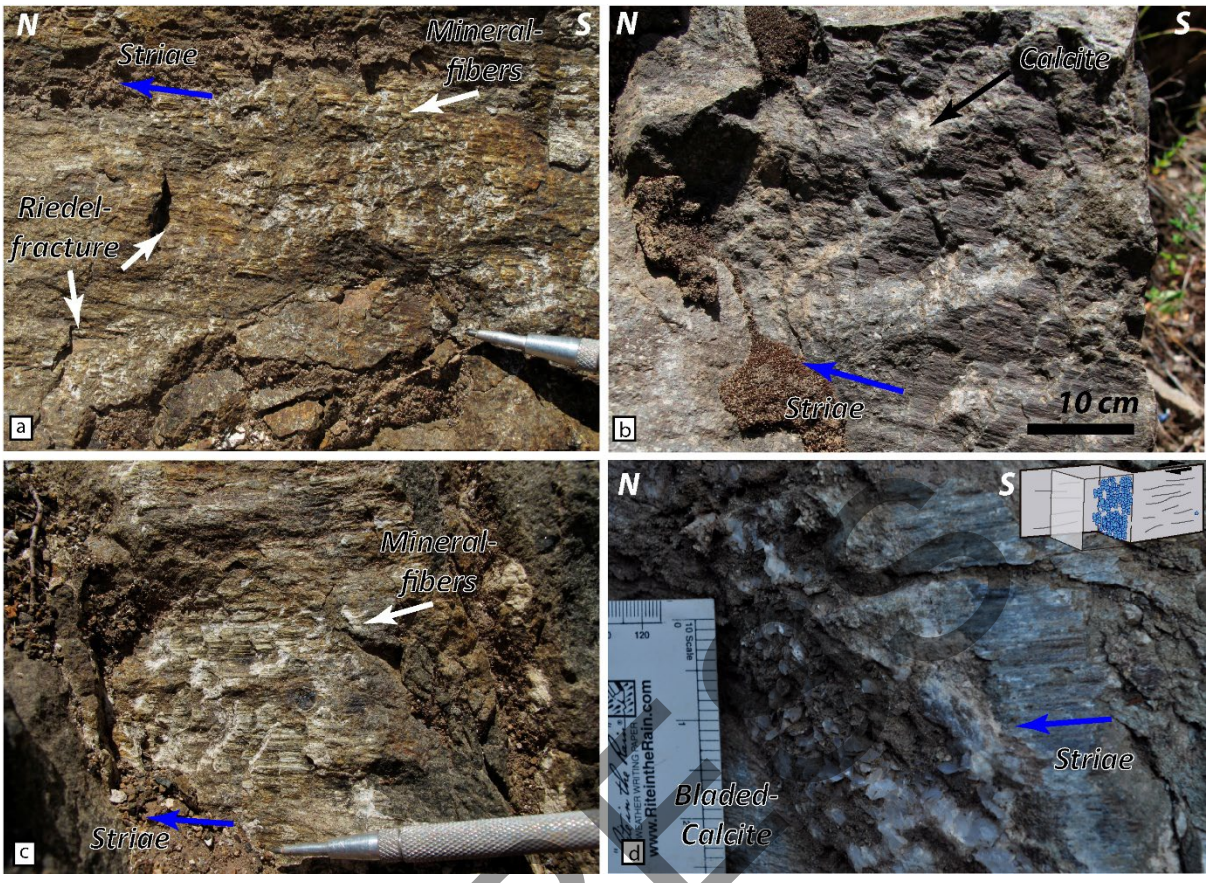

Fig. 5. Typical examples of mesoscopic fault surfaces with striae (slickensides) in the study area. These surfaces exhibit one or more of the following features: (**A**) dextral Riedel-type fractures and mineral fibers; (**B**) calcite precipitation behind fault steps; (**C**) zeolite slickenfibers; and (**D**) bladed-like calcite inside a dilatational jog (diagram provided for spatial context).

1471 ●

1472 ● **Fig. 6.** Summary cartoon illustrating the along- and across-strike segmentation in
1473 the geometry and kinematics of slip and deformation partitioning in the Southern
1474 Andes. All segments are bounded by south-verging, WNW- to NW-striking
1475 reverse faults/deformation zones, namely Maipo, Lanalhue, and Chacao. Black
1476 arrows roughly indicate approximate P directions (T axes are not shown for

1477 simplicity). The dotted patterns around the major segment boundary faults
1478 represent their approximate widths as deformation zones. The striped pattern
1479 associated with the LOFS marks the approximate region containing both master
1480 and subsidiary faults. See text for details.